Mechanical behaviour and energy evolution of polyurethane-mixed ballast under revised bonding constitutive model

Xiao, Hong; Ling, Xing; Wang, Meng; Fang, Shu Wei; Wang, Hao Yu

DOI
10.1016/j.conbuildmat.2021.126260

Publication date
2022

Document Version
Final published version

Published in
Construction and Building Materials

Construction and Building Materials 320 (2022) 126260

Contents lists available at ScienceDirect

Construction and Building Materials

journal homepage: www.elsevier.com/locate/conbuildmat

Mechanical behaviour and energy evolution of polyurethane-mixed ballast under revised bonding constitutive model

Hong Xiao [a,*], Xing Ling [a], Meng Wang [b], Shu-Wei Fang [c], Hao-Yu Wang [d]

[a] Beijing Key Laboratory of Track Engineering, Beijing Jiaotong University, Beijing, China
[b] China Academy of Railway Sciences Group Co., Ltd, Beijing, China
[c] Beijing Metro Operation Co., Ltd, Beijing, China
[d] Delft University of Technology, Delft ,Netherlands

ARTICLE INFO

Keywords:
Polyurethane-mixed ballast
Mechanical behaviour
Energy evolution
Constitutive model

ABSTRACT

The bonding contact presents complex modes in polyurethane-mixed ballast. The commonly used parallel bond model is revised and four different contact models are developed including Ballast-Ballast Contact Bonding, Ballast-Ballast Noncontact Bonding, Ballast-Sleeper Contact Bonding, and Ballast-Sleeper Noncontact Bonding. The mechanical behaviour and energy evolution of polyurethane-mixed ballast with various amounts of glue are studied from the macro and mesoscopic properties. Results show that the elastic strain energy has always been the main form in polyurethane-mixed bed, followed by viscous strain energy, frictional energy, and damping energy. Compared with the common ballast bed, there are more contacts in polyurethane-mixed ballast bed and, when more glue is used, the amount of contacts is further increased while the maximum contact force is reduced. After bonding, the amount of contacts is significantly increased and all forms of energy become more evenly distributed at different surfaces of the sleeper. The kinetic energy of polyurethane-mixed ballast fluctuates with smaller amplitude and convergences more quickly under cyclic loading, which is reflected in the macroscopic aspect that the settlement of polyurethane-mixed ballast bed is relatively small and can be fast completed.

1. Introduction

Polyurethane-mixed ballast is a new track structure wherein the ballast particles are bonded or glued by polyurethane binder [1–2]. After the reinforcement, the integrity and stability of the ballast bed are significantly improved. In China, it is mainly used in transition zones between ballast track and slab track, and it can also be used to prevent flying ballast in high-speed lines [3–6], as shown in Fig. 1. Besides, as a measure to improve the performance of common ballasted tracks, polyurethane-mixed ballast has significant effects in improving the resistance of the ballast bed and reducing degradation, which has also been used in weak links of railway track, such as curve, switch and crossing, and subgrade fracture zone[7–10].

In the past ten years, relevant research on polyurethane-mixed ballast has been developed rapidly. It has gradually expanded from the macro-mechanical properties to its *meso*-mechanical behaviour. The macro-mechanical properties mainly include the static and dynamic mechanical properties of polyurethane-mixed ballast, such as support stiffness, lateral/longitudinal resistance and vibration characteristics, etc. The *meso*-mechanical properties mainly focus on the bonding contact of ballast particles, including the contact force and the energy state at the contact point, etc. The researches have been conducted either in experimental or numerical ways, wherein the experimental researches include field tests and laboratory tests and numerical researches are conducted using the finite element method (FEM) or discrete element method (DEM). The relevant studies are summarised in appendix.

From the existed researches, it can be found that the current researches on the bonded ballast are mainly focused on macro-mechanical behaviour. However, its *meso*-mechanical behaviour is relatively lacking. Compared with the common ballast, the bonded ballast forms a whole due to the bonding effect of glue, and thus its macro-mechanical behaviour is changed significantly. The most fundamental reason for this is the change of contact state, which is at the *meso*-level. In the bonded ballast, the ballast particles are connected in a complex way. There are not only compressive force between particles, but also other various types of loads, such as shear, bending, torsion, and tensile force [39,42,64,65,66]. Because the contact between ballast particles is changed by the glue at the *meso*-level, the distribution of train load

* Corresponding author.
E-mail address: xiaoh@bjtu.edu.cn (H. Xiao).

https://doi.org/10.1016/j.conbuildmat.2021.126260
Received 14 September 2021; Received in revised form 10 November 2021; Accepted 27 December 2021
Available online 5 January 2022

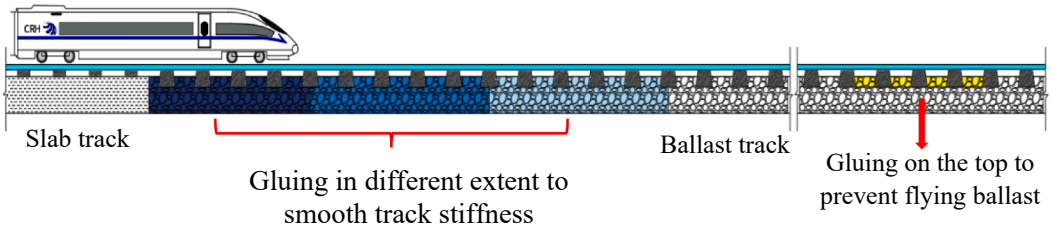

Fig. 1. Major application of high speed railway in China.

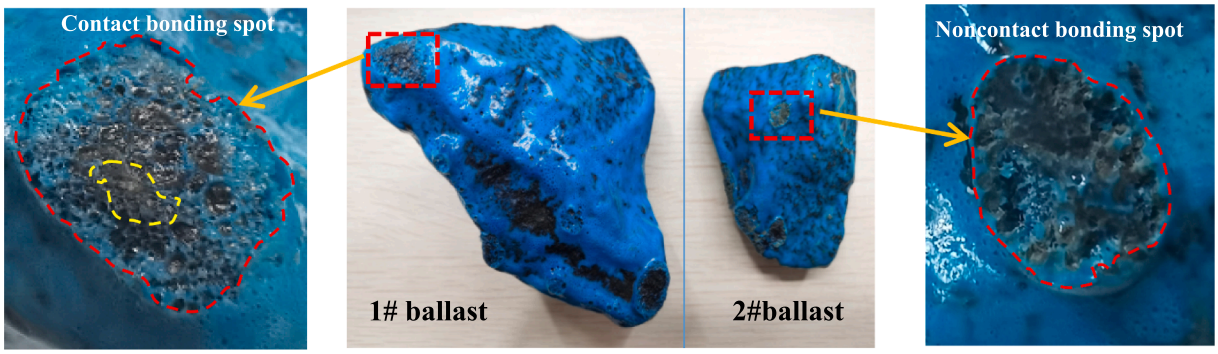

Fig. 2. Surface bonding layer and spots of ballast particles. (The spots are on a scale visible to the naked eye).

inside the ballast bed is different, which leads to the changes in the macro-mechanical behaviour. Therefore, in order to discover the macro-mechanical behaviour of the bonded ballast, it is necessary to study the contact between the ballast particles, in the process of which proposing a reasonable constitutive model of the bonded ballast is the key. After that, because the *meso*-mechanism behaviour of the bonded ballast is essentially the process of storage and dissipation energy, this paper conducts the research from the energy point of view.

2. Constitutive model of glue bond and its modification

2.1. Bonding spots on the surface of ballast particles

After spraying glue, the glue (polyurethane) forms a bonding layer on the surface of ballast particles, and at the same time forms complex bonding spots [1]. According to the initial contact state and the morphological characteristics of bonding spots, the bonding spots can be divided into two categories. Contact bonding is when there is the initial contact between ballast particles and the glue forms bonding spots around the original contact points. Noncontact bonding is when there is a gap between ballast particles and the glue fills the gap with bonding spots. Fig. 2 shows the two types of bonding spots, wherein two ballast particles (in black) are covered by glue (in blue). Ballast particle 1 has a bonding spot of the contact bonding, in which a non-bonded core inside the bonding spot can be seen. Ballast particle 2 has a bonding spot of the noncontact bonding, in which the bonding spot is completely bonded. The pictures of the bonding spot of the contact bonding can be also found in [1].

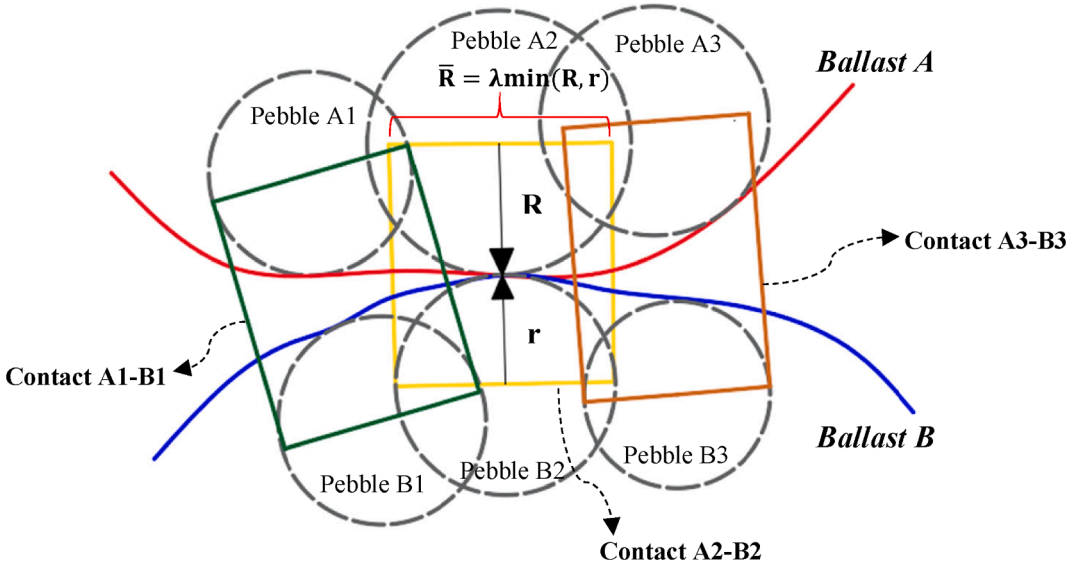

Fig. 3. Schematic diagram of bonding contacts.

2.2. Parallel bond model and its shortcomings

Because the change of mechanical behaviour of the bonding ballast originates from the change in the contact between ballast particles, developing a precise bond model is crucial for the analysis. The parallel bond model [39] has been widely adopted for modelling the bonding ballast, because it allows simultaneous simulation of compression, tension, bending, shear, and torsion at contact points, which can exactly reflect the characteristics of bonded ballast particles. The model has been used in [5,15,38] to simulate the bonding effect of glue. The contact relationship between two bonded ballast particles when using the parallel bond model is shown in Fig. 3.

When simulating ballast particles using the discrete element method, it is necessary to consider the effect of the irregular shape of the particles on the mechanical behaviour of the ballast bed [40–41]. For irregular ballast particles, the bubble-pack algorithm is generally used in discrete element modelling to fill the contours of particles with small spheres [39]. Pebble A1, Pebble A2, and Pebble A3 in Fig. 3 are the local filling for Ballast A, while Pebble B1, Pebble B2, and Pebble B3 for Ballast B. Contact A1-B1, Contact A2-B2, and Contact A3-B3 are the three parallel bond contacts between Ballast A and Ballast B.

Taking Contact A2-B2 as an example, when Pebble A2 and Pebble B2 have an initial contact and later become bonded, the new bonding contains two parts: the initial non-bonded contact and the bonded contact. The contact force F_c and torque M_c can be calculated as follows [39].

$$F_c = F_l + F_d + F_b \tag{1}$$

$$M_c = M_{pb} \tag{2}$$

Where F_l is the linear contact force, F_d is the damping force, F_b is the bonding contact force, and M_{pb} is the parallel bonding moment.

For the linear contact part, the linear contact force F_l includes the normal contact force and the tangential contact force. The increment ΔF_{ln} of the normal contact force and the increment ΔF_{ls} of tangential contact force can be calculated as follows [39]:

$$\Delta F_{ln} = k_n \Delta\delta_n \tag{3}$$

$$\Delta F_{ls} = k_s \Delta\delta_s \tag{4}$$

Where k_n and k_s are the linear contact stiffness in the normal and tangential direction, respectively; $\Delta\delta_n$ and $\Delta\delta_s$ are the increments of relative displacement in the normal and tangential, respectively.

When the tangential force continues to increase, in the case of relative slippage occurs between particles, the tangential force F_{ls} and the normal force F_{ln} can be expressed as follow[39].

$$F_{ls} = \mu F_{ln} \tag{5}$$

where μ is the friction coefficient of the contact point.

The elastic strain energy E_k stored during the linear contact can be calculated as follows[39]:

$$E_k = \frac{1}{2}\left(\frac{F_{ln}^2}{k_n} + \frac{F_{ls}^2}{k_s}\right) \tag{6}$$

ΔE_u is the increment of the energy dissipation caused by the relative slippage between ballast particles can be calculated as follows[39].

$$\Delta E_u = F_{ls} \cdot \Delta\delta_{s\mu} \tag{7}$$

Where $\Delta\delta_{s\mu}$ is the increment of the tangential frictional slippage.

For the damping contact part, damping force F_d is generated by the viscous damping between ballast particles, which includes the normal damping force F_{dn} and tangential damping force F_{ds}[39].

$$F_{dn} = c\delta_{nv} \tag{8}$$

$$F_{ds} = c\delta_{sv} \tag{9}$$

Where c is the viscous damping coefficient, δ_{nv} and δ_{sv}, are the relative moving speeds in the normal and tangential directions, respectively.

The corresponding increment of the energy dissipation caused by damping ΔE_d can be calculated as follows [39].

$$\Delta E_d = F_d \cdot (\Delta\delta_n + \Delta\delta_s) \tag{10}$$

For the bonded contact part, the increment of the bonding contact force ΔF_{bn} (normal) and ΔF_{bs}(tangential), the increment of torque ΔM_t, and the increment of bending moment ΔM_b can be calculated as follow [39].

$$\Delta F_{bn} = k_{bn} \cdot A_b \cdot \Delta\delta_n \tag{11}$$

$$\Delta F_{bs} = k_{bs} \cdot A_b \cdot \Delta\delta_s \tag{12}$$

$$\Delta M_t = k_{bs} \cdot J \cdot \Delta\theta_t \tag{13}$$

$$\Delta M_b = k_{bn} \cdot I \cdot \Delta\theta_b \tag{14}$$

Where k_{bn} is the normal stiffness of the parallel bonding; k_{bs} is the tangential stiffness of parallel bonding; k_{bn} and k_{bs} can be converted by a certain stiffness ratio η ($k_{bn}/k_{bn} = \eta$); A_b is the area of the section of the parallel bonding; J is the polar moment of inertia of the parallel bonding; I is the moment of inertia of section of the parallel bonding; $\Delta\theta_t$ is the increment of the torsional angular displacement; $\Delta\theta_b$ is the increment of the bending angular displacement.

The viscous strain energy stored by the parallel bonding can be calculated as follows[39].

$$E_b = \frac{1}{2}\left(\frac{F_{bn}^2}{k_{bn} \cdot A_b} + \frac{F_{bs}^2}{k_{bn} \cdot A_b} + \frac{M_t^2}{k_{bs} \cdot J} + \frac{M_b^2}{k_{bs} \cdot I}\right) \tag{15}$$

As can be seen from above, there exist linear force, damping force and bonding contact force between the bonded ballast particles when the parallel bond model is in use, the combination of which leads to a complex transfer mode of train loads in the bonded ballast. Therefore, it is crucial to calculate the three force accurately in the constitutive model. Among the three, the calculation of the linear contact force and damping force is relatively clear, while the calculation of bonding contact force is complicated due to the multiple contact parameters involved.

For Contact A2-B2, the bonding contact is formed between Pebble A2 and B2, wherein the radius R of Pebble A2 is larger than the radius r of Pebble B2. The bonding radius between Pebble A2 and B2 is determined both by smaller radius r and radius magnification λ [39]. In Contact A2-B2, the radius of the bonding R_b, the area of the bonding A_b, the normal stiffness of bonding k_{bn}, and the tangential stiffness of bonding k_{bs} can be calculated as follows [39].

$$R_b = \lambda min(R, r) \tag{16}$$

$$A_b = \pi R_b^2 \tag{17}$$

$$k_{bn} = \bar{k}_{bn} A_b \tag{18}$$

$$k_{bs} = \bar{k}_{bs} A_b \tag{19}$$

Where $\bar{k}_{bn}$ and $\bar{k}_{bs}$ is the normal and tangential bonding stiffness per unit of the bonding area.

As shown in Equation (16)-(19), the normal and tangential bonding stiffness of Contact A2-B2 are related to the radii of Pebble A2 and Pebble B2. It is remarkable to note that Pebble A2 and Pebble B2 are used to fill irregular ballast (Ballast A and B respectively). Their radii are determined by the ballast morphological characteristics and the bubble-pack algorithm [39], which means they are irrelevant with the bonding behaviour. As a result, according to Equation (16), it can be inferred that the radius of the bonding area R_b is obtained by adjusting the dimension that are not related to the ballast bonding, which makes the bonding area A_b achieved from Equation (17) having no physical meaning, and

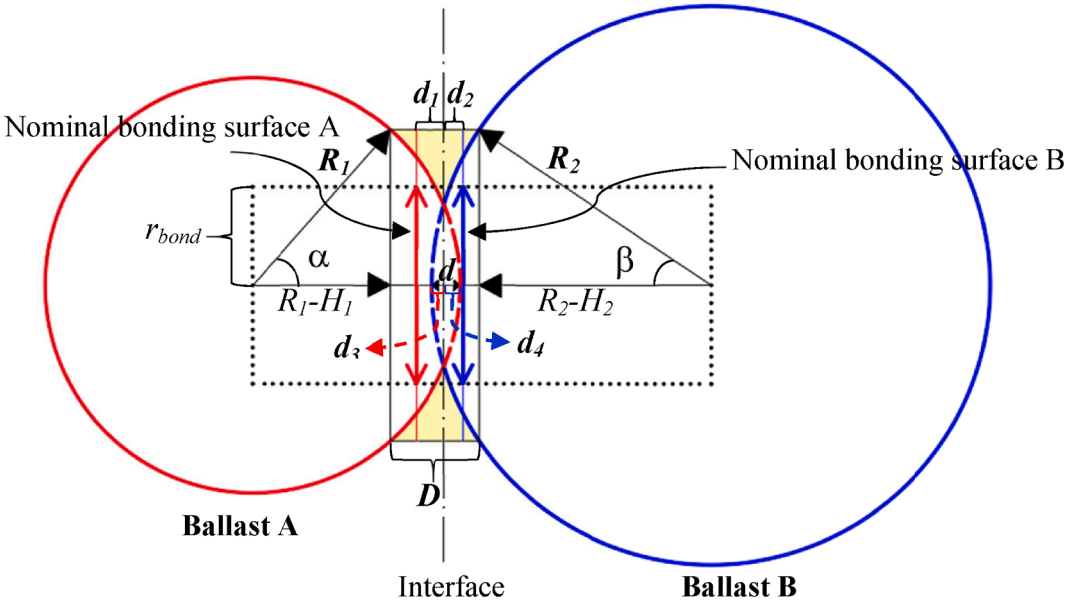

Fig. 4. Ballast-Ballast Contact Bonding.

same for the bonding stiffness k_{bn} and k_{bs} from Equation (18) and (19). Furthermore, the rationality of the contact force and viscous strain energy calculated from Equation (11)-(15) will also be affected.

In the existing researches, the parallel bond model is not only used for the analysis of the bonding effect between ballast particles but also for the analysis of the effect of the amount of glue. For instance, various amount of glue is considered by changing the bonding radius in [16,37], while by changing the viscous contact stiffness in [1]. Based on the results of existing studies, it can be found that it is successful to analyse the macroscopic properties of bonding ballast, such as the lateral resistance and settlement of the ballast bed. However, there are some defects in the mesoscopic aspects including distribution of contact force and proportion of main energy etc., which has not been improved in the existing DEM models.

The defects can be attributed to three aspects: (1) The increase in the amount of ballast glue will not only strengthen the bonding between the ballast particles, but also increase the amount of bonding contact. (2) The mechanical behaviour of the bonding between ballast particles are not only related to the properties of the glue, but also related to the state of the ballast bed, such as gradation and compactness. Therefore, the state of the ballast bed should also be reflected in the parallel bond constitutive model. (3) The bonding force between ballast particles at the *meso*-level needs to have a clear physical meaning. To overcome these defects, this paper modifies the parallel bond model for the bonding ballast.

2.3. Modification for the parallel bond model

During the process of making bonding ballast, the glue is sprayed on the ballast bed and attaches to the surface of ballast particles. Because the thickness of the bonding layer is much smaller than the size of the ballast particles, the bonding layer can be considered as evenly distributed on ballast particles [64]. The thickness of the bonding layer and the gap between ballast particles together determine the behaviour of ballast bonding.

The thickness of the bonding layer can be calculated according to the amount of glue and the surface area of ballast particles using the following equation.

$$d = \frac{M}{\rho \sum S_i} \tag{20}$$

Where: d is the thickness of the bonding layer, M is the mass of the ballast glue, ρ is the density of the ballast glue, and S_i is the surface area of a single ballast particle.

After getting the thickness of the bonding layer by Equation (20), the critical size of ballast bonding D can be expressed as follows:

$$D = 2d \tag{21}$$

The critical size of ballast bonding can be used as the boundary condition of bonding type I, and as the criterion for determining the bonding type II at a contact spot as well. Therefore, combined with Equation (20)-(21), the relationship between the amount of ballast glue (the macroscopic aspect) and the bonding state (the mesoscopic aspect) is founded.

In the discrete element model of the bonding ballast, the contact between two ballast particles is considered as the contact between two spheres, and the contact between a ballast particle and a sleeper as the contact between a sphere and a plane.

Combining the findings of the research on the bonding behaviour of various types of granular materials in [42,64] and the two types of bonding spots (Fig. 2), the bonding contact in the discrete element model can be divided into four categories according to the initial contact state and contact objects, which are Ballast-Ballast Contact Bonding, Ballast-Ballast Noncontact Bonding, Ballast-Sleeper Contact Bonding, and Ballast-Sleeper Noncontact Bonding.

(a) Ballast-Ballast Contact Bonding

When two ballast particles are initially contacted and then bonded, the bonding is shown in Fig. 4.

In Fig. 4, Ballast A and Ballast B have initial contact with an overlap, the thickness of which is d. The glue is filled around the overlap (in yellow) and the maximum thickness of the bonding is the critical size of ballast bonding D. Taking the middle of the overlap as the interface, the bonding can be divided into two parts. The equivalent bonding thickness is d_1 and d_2 for Ballast A and B respectively, wherein d_1 and d_2 are taken as half of the distance between the interface to the maximum thickness. The surface on the left of the interface with a distance of d_1 is considered as Nominal bonding surface A and that on the right of the interface with a distance of d_2 as Nominal bonding surface B. Therefore, the distance between nominal bonding surface A and B can be calculated as follow.

$$d_1 + d_2 = \frac{D}{2} \tag{22}$$

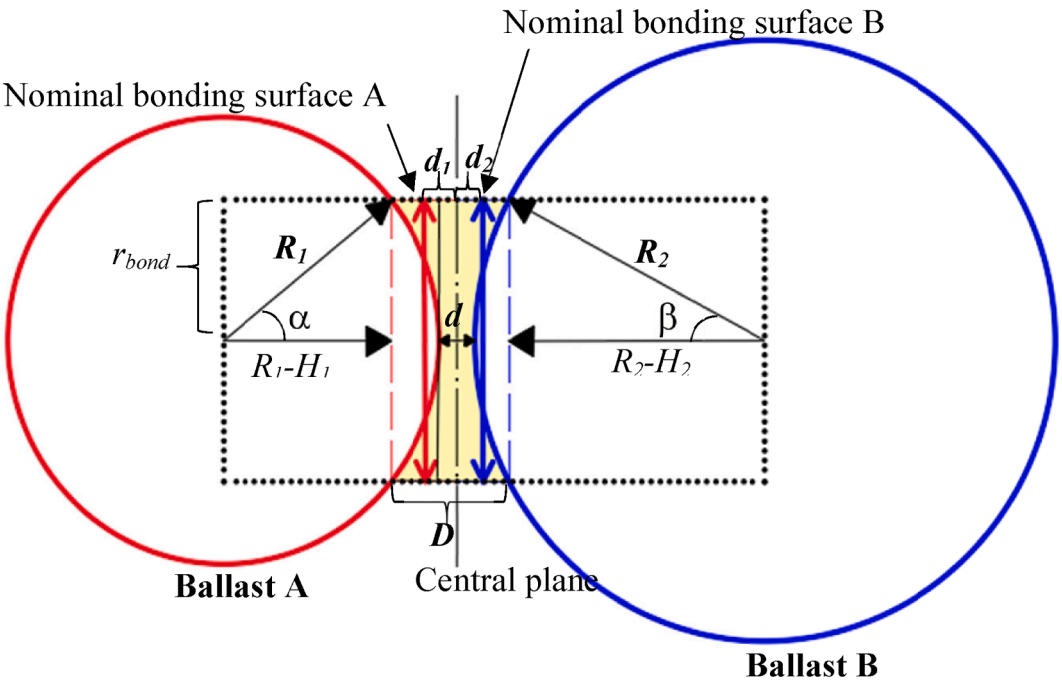

Fig. 5. Ballast-Ballast Noncontact Bonding.

Because the ballast glue is bonded around the overlap in a ring shape, the area of the bonding is equivalent to a round with a radius of r_{bond}. The area of the overlap satisfies the following equations.

$$R_1^2 - (R_1 - d_4)^2 = R_2^2 - (R_2 - d_3)^2 \tag{23}$$

$$d_3 + d_4 = d \tag{24}$$

$$h = [R_1^2 - (R_1 - d_4)^2]^{1/2} \tag{25}$$

Where: R_1 and R_2 are the radius of the Ballast particle A and B, respectively; d_3 is the maximum distance from the interface to Ballast particle B; d_4 is the maximum distance from the interface to Ballast particle A; h is the radius of the boundary circle at the overlap.

The area of the boundary circle at the overlap $S_{overlap}$ can be calculated using Equation (23)-(25) as:

$$S_{overlap} = \pi h^2 \tag{26}$$

Also, the overlap area and the bonding area meet the following relationships.

$$R_1^2 - (R_1 - H_1)^2 = R_2^2 - (R_2 - H_2)^2 \tag{27}$$

$$H_1 + H_2 = D + d \tag{28}$$

According to Equation (27)-(28), the sum of the overlap area S_{total} and the bonding area can be calculated as follows.

$$S_{total} = \pi(R_1 sin\alpha)^2 = \pi \cdot (R_2 sin\beta)^2 \tag{29}$$

Where $sin\alpha = [1 - (1 - H_1/R_1)^2]^{1/2}$ and $sin\beta = [1 - (1 - H_2/R_2)^2]^{1/2}$。

According to Equations (26) and (29), the equivalent bonding area S_{bond} can be calculated as follows.

$$S_{bond} = S_{total} - S_{overlap} = \pi r_{bond}^2 \tag{30}$$

In this way, the irregular shape of the ballast glue filled between particles can be converted to a regular cylindrical shape between two nominal bonding surfaces. The cross-sectional area of the equivalent cylinder is marked as S_{bond} and the thickness of the equivalent cylinder D/2.

It should be noted that the bonding stiffness in this paper refers to the effective modulus of the ballast glue, based on which the normal bonding stiffness can be obtained. When the nominal bonding surfaces are not used, considering the effective modulus of the ballast glue as E*, the normal bonding stiffness between ballast particles $\bar{k}_{n0}$ can be calculated as follows [39].

$$\bar{k}_{n0} = \frac{\pi E^* R_1^2}{R_1 + R_2} \tag{31}$$

In order to consider the bonding behaviour between ballast particles, the stiffness in Equation (31) is modified by the parameters related to the nominal bonding surface and the modified normal bonding stiffness $\bar{k}_{n1}$ can be expressed as follows.

$$\bar{k}_{n1} = \frac{2E^* S_{bond}}{D} \tag{32}$$

It can be seen from Equation (32) that, for the Ballast-Ballast Contact Bonding, the modified normal bonding stiffness is directly relevant to the bonding state between ballast particles, which increases with the bonding area. After this modification of normal bonding stiffness and bonding area, other parameters in the parallel bonding constitutive model, including bonding force, bonding torque, and bending moment, can be also modified using Equation (11)-(14).

(b) Ballast-Ballast Noncontact Bonding

When there is no initial contact between ballast particles, the ballast glue forms a bonding contact between the ballast particles as shown in Fig. 5.

As seen from Fig. 5, there is an initial distance between two ballast particles d. When the glue is filled between the ballast particles, the minimum thickness of the bond area is d and the maximum thickness is the critical size of ballast bonding D. Because the gap is irregular in the Ballast-Ballast Noncontact Bonding, the bonding area can be also considered as an equivalent cylinder. Using the central plane of two ballast particles as the interface, the bonding area can also be divided into two parts. In the same way as used the above section, the equivalent bonding thickness is d_1 and d_2 and the Nominal bonding surface A and B can be also defined for Ballast particle A and B respectively. Thus, the width of the equivalent bonding area can be calculated as follows.

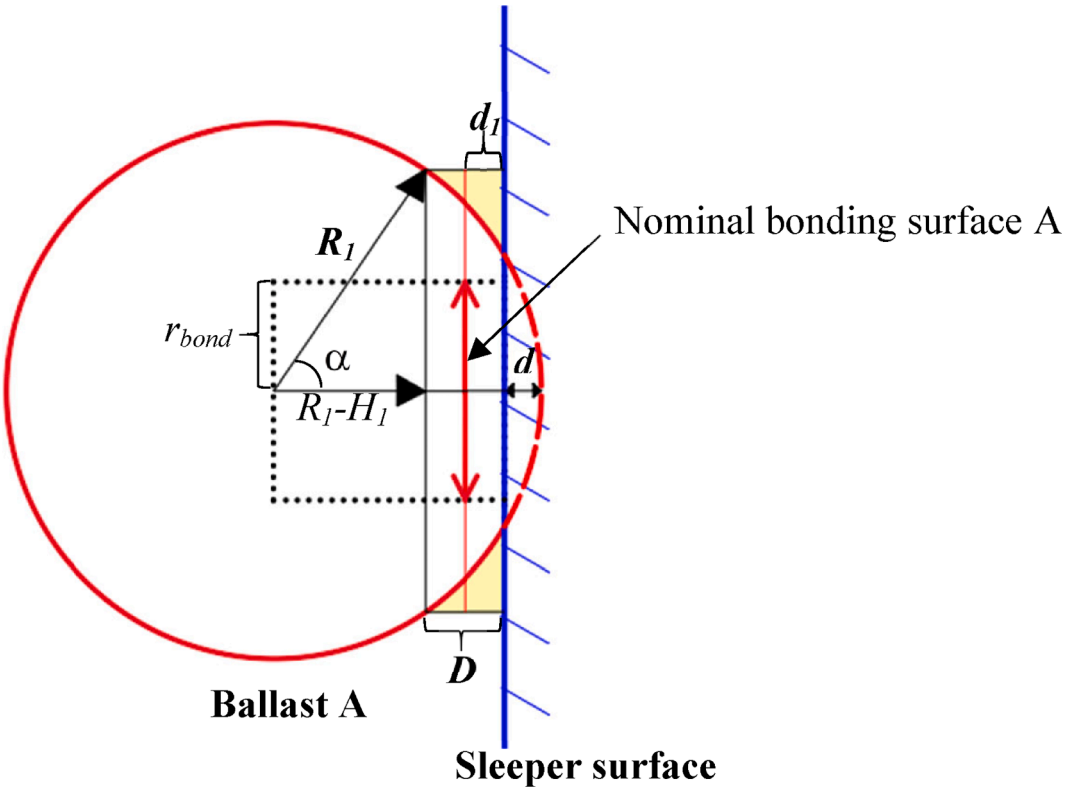

Fig. 6. Ballast-Sleeper Contact Bonding.

$$d_1 + d_2 = \frac{D+d}{2} \tag{33}$$

For the Ballast-Ballast Noncontact Bonding, the radius of the equivalent cylindrical bonding area is determined by the bonding area, the following equations can be derived.

$$R_1^2 - (R_1 - H_1)^2 = R_2^2 - (R_2 - H_2)^2 \tag{34}$$

$$H_1 + H_2 = D - d \tag{35}$$

Where the definitions of H_1 and H_2 are the same as the Ballast-Ballast Contact Bonding.

Using Equation (34) and (35), the equivalent bonding area S_{bond} can be calculated as follows:

$$S_{bond} = \pi(R_1 \cdot sin\alpha)^2 = \pi(R_2 \cdot sin\beta)^2 = \pi r_{bond}^2 \tag{36}$$

Where the definitions of $sin\alpha$ and $sin\beta$ are the same as the Ballast-Ballast Contact Bonding.

Thus, the modified normal bonding stiffness $\bar{k}_{n1}$ for the Ballast-Ballast Noncontact Bonding can be expressed as follows.

$$\bar{k}_{n1} = \frac{2E^* S_{bond}}{D+d} \tag{37}$$

It can be seen from Equation (37) that for the Ballast-Ballast Noncontact Bonding, the modified bond stiffness also increases with the bonding area, while decreases with the gap between ballast particles. In the same way, the bonding force, bonding torque, and bending moment can be calculated using Equation (11)-(14).

(c) Ballast-Sleeper Contact Bonding

When there is an initial contact between a ballast particle and a sleeper, the ballast glue forms bonding around the contact area, as shown in Fig. 6.

As seen in Fig. 6, there is an overlap between Ballast A and the sleeper, the thickness of which is referred to as d. The ballast glue surrounds the overlap in a ring shape and the maximum thickness is the critical size of ballast bonding D.

Similar to the Ballast-Ballast Contact Bonding, the bonding area can also be converted to a regular cylindrical shape. Nominal bonding surfaces A can be also defined and consequently the equivalent bonding thickness d_1 can be defined as the distance between the sleeper surface and Nominal bonding surfaces A, as shown in Equation (38).

$$d_1 = \frac{D}{2} \tag{38}$$

Since the ballast bonding is in a ring shape around the overlap between Ballast particle A and the sleeper surface, the following geometric relationship can be derived.

$$R_1^2 = (R_1 - d)^2 + h^2 \tag{39}$$

Where: h is the radius of the boundary circle of the overlap.

The area of the boundary circle at the overlap $S_{overlap}$ can be calculated as follow.

$$S_{overlap} = \pi h^2 \tag{40}$$

After that, the sum of the overlap area and bonding area meets the following relationships.

$$H_1 = D + d \tag{41}$$

$$S_{total} = \pi[R_1^2 - (R_1 - H_1)^2] \tag{42}$$

Therefore, the bonding area can be calculated as follows.

$$S_{bond} = S_{total} - S_{overlap} = \pi r_{bond}^2 \tag{43}$$

When the nominal bonding surface is not considered, the normal bonding stiffness between a ballast particle and a sleeper $\bar{k}_{n0}$ can be calculated as follows

$$\bar{k}_{n0} = \pi E^* R_1 \tag{44}$$

After considering the nominal bonding surfaces, the modified normal

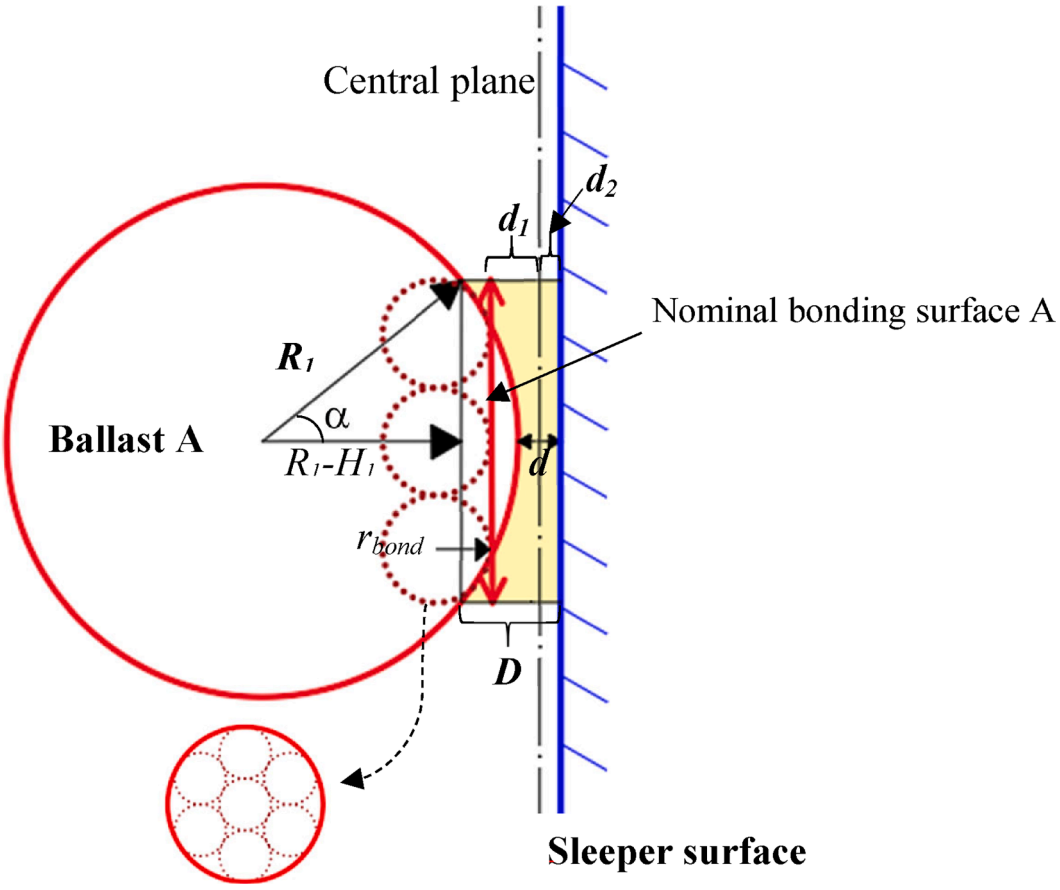

Fig. 7. Schematic diagram of the Ballast-Sleeper Noncontact Bonding.

bonding stiffness $\bar{k}_{n1}$ is as follow.

$$\bar{k}_{n1} = \frac{2E^* S_{bond}}{D} \tag{45}$$

It can be seen from Equation (45) that the modified bonding stiffness increases with the cross-sectional area of the equivalent cylinder in the Ballast-Sleeper Contact Bonding. In the same way as above, the bonding force, bonding torque, and bending moment can be modified using Equation (11)-(14).

(d) Ballast-Sleeper Noncontact Bonding

When there is no initial contact between a ballast particle and a sleeper, the ballast bonding is formed between the ballast particle and sleeper, as shown in Fig. 7.

Since there is an initial distance d between Ballast A and the sleeper surface, the minimum thickness of the ballast bonding is d and the maximum thickness is the critical size of ballast bonding D. Using the middle point of the minimum thickness d, the center plane can be defined, which divides the bonding area into two parts. The equivalent bonding thickness of Ballast particle A is referred to as d_1 and the plane where d_1 is located is as Nominal bonding surface A. The equivalent bonding thickness of the sleeper surface is referred to as d_2. They meet the following equations.

$$H_1 = D - d \tag{46}$$

$$d_1 = \frac{d + H_1}{2} \tag{47}$$

$$d_2 = \frac{d}{2} \tag{48}$$

The equivalent bonding thickness can be calculated as follow.

$$d_1 + d_2 = \frac{D + d}{2} \tag{49}$$

As a new type of contact, the Ballast-Sleeper Noncontact Bonding is especially important in the modelling because two following reasons.

The first is that the contact is used to transfer the train load from sleepers directly. The second is that the bonding behaviour is mainly determined by the ballast glue. Therefore, the correct modelling of the Ballast-Sleeper Noncontact Bonding is crucial for the study. In this paper, the local refinement method is used to further refine the equivalent cylindrical bonding area of the Ballast-Sleeper Noncontact Bonding. As shown in Fig. 7, after repeated trial calculations, 7-ball mode is used to densely fill the bonding area, so that 7 juxtaposed bonding contacts are formed on Nominal bonding surface A, which refines the ballast bonding. It should be noted that, in fact, the local refinement method can be used for other types of bonding contacts, but this will seriously affect the calculation efficiency of the discrete element model. As a compromise, this paper only refines the Ballast-Sleeper Noncontact Bonding.

After using the local refined method, the bond radius of the Ballast-Sleeper Noncontact Bonding satisfies the following relationship:

$$r_{bond} = R_1 \cdot sin\alpha/3 = \left[R_1^2 - (R_1 - H_1)^2\right]^{1/2}/3 \tag{50}$$

From Equation (49), the area of the bonding area can be calculated as follows:

$$S_{bond} = \pi r_{bond}^2 \tag{51}$$

When the nominal bonding surface is not considered, the normal bonding stiffness between a ballast particle and a sleeper $\bar{k}_{n0}$ is as follows.

Table 1
Modified normal bonding stiffness.

Type	Modified normal bonding stiffness/$\overline{k}_{n1}$
Ballast-Ballast Contact Bonding	$\frac{2E^*S_{bond}}{D}$
Ballast-Ballast Noncontact Bonding	$\frac{2E^*S_{bond}}{D+d}$
Ballast-Sleeper Contact Bonding	$\frac{2E^*S_{bond}}{D}$
Ballast-Sleeper Noncontact Bonding	$\frac{2E^*S_{bond}}{D+d}$

Table 2
Parameters in the DEM model.

Parameters	Value
Linear normal contact stiffness	50 MN/m
Linear tangential contact stiffness	33 MN/m
Friction coefficient	0.5
Effective bonding modulus	39 MPa (Glue 48 kg/m^3)19 MPa (Glue 33 kg/m^3)
Normal/tangential bonding contact damping ratio	0.15 (Glue 48 kg/m^3)0.10 (Glue 33 kg/m^3)0.01 (Glue 0)
Normal tangential stiffness ratio	1.5

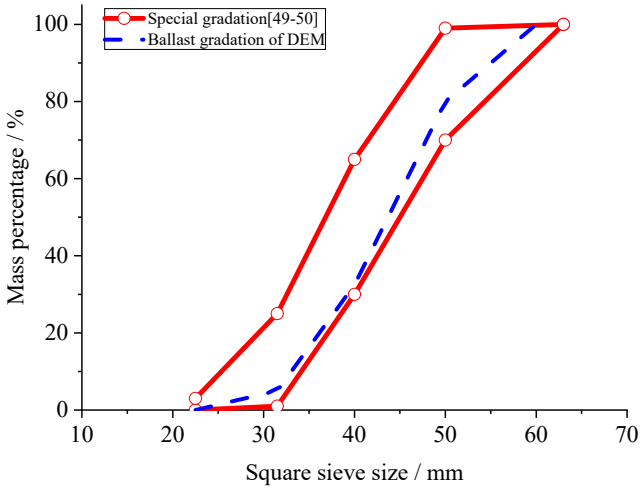

Fig. 8. Ballast gradation.

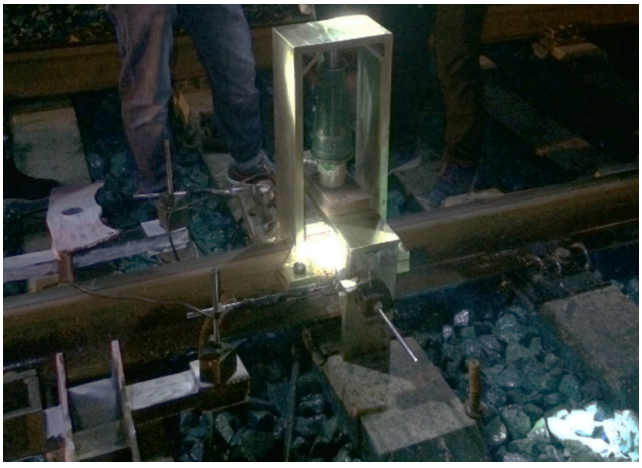

Fig. 10. Field tests.

$$\overline{k}_{n0} = \pi E^* r_{bond} \tag{52}$$

After modification, the normal stiffness is calculated as follows.

$$\overline{k}_{n1} = \frac{2E^* S_{bond}}{D+d} \tag{53}$$

It can be seen from Equation (53) that the bond stiffness increases with the cross-sectional area of the equivalent cylinder and decreases with the gap. Similar to above, the bonding force, bonding torque, and bending moment can be modified using Equation (11)-(14).

For the different constitutive relations, it can be found that the normal bonding stiffness is the most key parameter, and other parameters can be further obtained according to the normal bonding stiffness. The normal bonding stiffness corresponding to the four modified bond constitutive models is summarized as shown in Table 1.

At this point, this article comprehensively considers three factors for the modification of the constitutive model of parallel bonding, including the distribution of ballast glue, the effect of ballast bonding on ballast particles, and the physical meaning of the ballast bonding at the *meso*-level. The modified bonding models are suitable for four different bonding types in the bonding ballast.

3. DEM model of bonding ballast

3.1. Model development

Ballast box test is developed using the DEM to analyse the energy evolution in bonding ballast. According to the present numerical simulations and laboratory tests [43–45], the size of the box is defined as 600 mm (length), 350 mm (width), and 500 mm (height). Because the irregularity of ballast particles and the gradation of ballast have a significant influence on the mechanical behaviour of ballast bed [46–48], the special gradation of the high-speed railway in China [49–50] is adopted. The gradation is shown in Fig. 8.

This paper uses the laser scanning method to obtain the shape of irregular ballast particles. Considering the diversity of the morphological characteristics, scanned ballast particles contain three shapes, which are cubic, long, and flat. The content of cubic ballast particles is

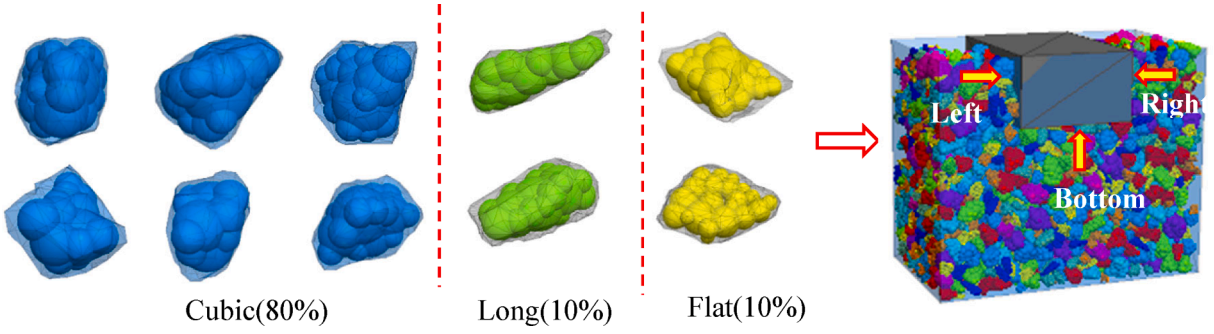

Fig. 9. DEM model for the box test.

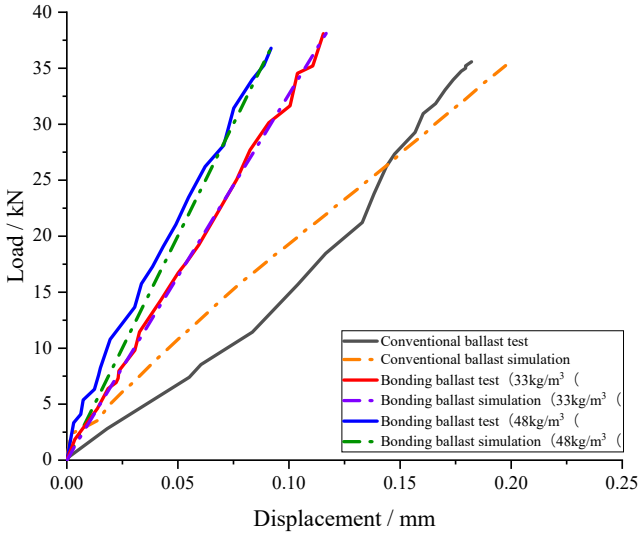

Fig. 11. Model validation (Field test results are from [1637]).

80% and that of long and flat ballast particles are both 10% in the model [49,51]. The developed model is shown in Fig. 9. The sleeper is modelled by the wall element, which is optimal to simulate the discrete contact with ballast particles [40,52].

3.2. Meso-parameter calibration and model verification

Considering the modified constitutive model of parallel bonding, the parameters of the conventional ballast bed have been first calibrated. After that, two types of ballast bonding with the amount of ballast glue 33 kg/m^3 and 48 kg/m^3 have been modelled. The parameters used in the model is shown in Table 2.

The comparison of numerical results and on-site test results (see Fig. 10) in three cases with 0, 33 kg/m^3, and 48 kg/m^3 glue is shown in Fig. 11. As seen in Fig. 11, the simulated results of the DEM model match well with the results of field tests. Therefore, the DEM model is used for further analysis in the paper.

4. Numerical simulations

4.1. Loads of high-speed trains

Sleepers in ballast tracks share various proportions of the train loads during trains passing. Following the sharing proportion and train loading model discussed in [53–56], the loading process is fitted using the Gaussian function. The loading history of a single axle is expressed as follows.

$$p(v,t) = P_0 A e^{-\frac{(vt)^2}{2w^2}} \tag{54}$$

Where P_0 is the axle load of the train, v is the operating speed of the train, t is the time, and A and w are fitting parameters.

It is commonly considered that the train load is carried by 5 sleepers under wheels with the sharing proportion of 0.1: 0.2: 0.4: 0.2: 0.1, according to [57–58]. Therefore, Equation (54) can be rewritten as follow.

$$p(v,t) = 0.36 P_0 e^{-\frac{(vt)^2}{0.78}} \tag{55}$$

The parameters of the commonly used high-speed trains in China (CRH3) are used in the simulation, which are 2.5 m as the distance between two wheels in a bogie and 17 t as the axle load. Because there is an overlap of the two wheel loads in a bogie, while loads of two bogies are independent, the load of a bogie is considered as the minimum loading cycle [58]. A minimum loading cycle is expressed as Equation (56) after considering the superposition of loads.

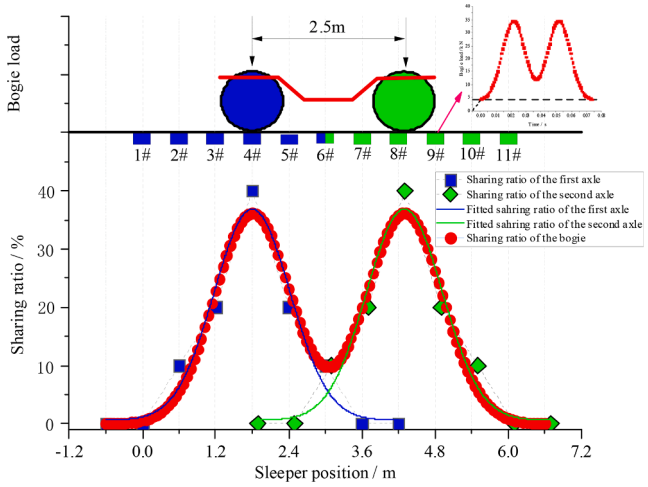

Fig. 12. Minimum loading cycle.

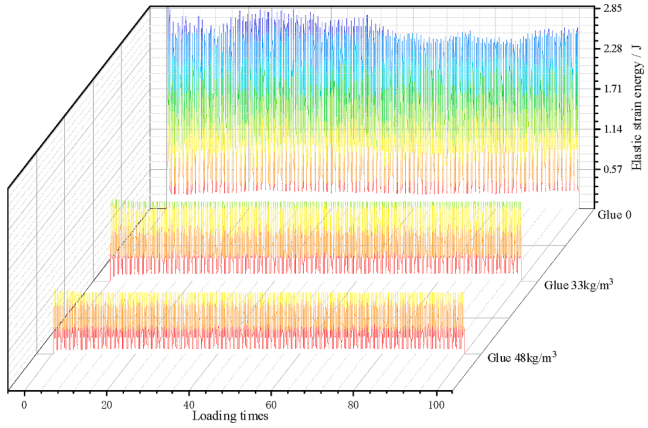

Fig. 13. Elastic strain energy evolution.

$$p(v,t) = 0.36 P_0 (e^{-\frac{(vt-1.8)^2}{0.78}} + e^{-\frac{(vt-4.3)^2}{0.78}}) \tag{56}$$

The loading history of the minimum loading cycle used in this paper is shown in Fig. 12, wherein a range of 11 sleepers (corresponding to 6.1 m = 1.8 m + 2.5 m + 1.8 m) is considered.

When the CRH3 high-speed train operates at a speed of 300 km/h, the loading period T is 0.0732 s (=6.1 m/300 km/h). The load applied on the ballast during a loading cycle can be expressed as:

$$f(t) = \frac{1}{2} p(v,t) + f_{const} \tag{57}$$

where v is 83.3 m/s, t ∈ [0, T]; f_{const} is the load constant, which is determined by the pressure caused by the weight of the track structure and set as 4 kN following [59–60].

4.2. Energy in ballast beds

4.2.1. Energy evolution of different forms

Energy evolution is always accompanied during the cyclic loading of high-speed trains. The results after 100 loading cycles are analysed to study energy evolution in the conventional and bonding ballast, as shown from Fig. 13 to Fig. 16.

As seen from Fig. 13 to Fig. 16, there is a significant difference in energy evolution between the conventional ballast and the bonding ballast.

As shown in Fig. 13, the elastic strain energy in the conventional

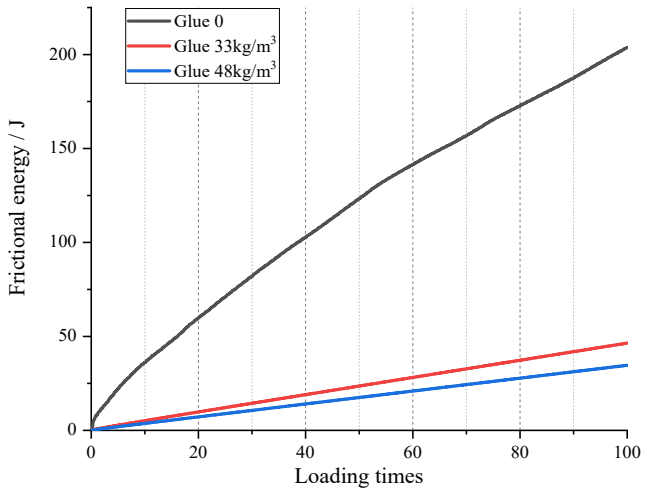

Fig. 14. Frictional energy evolution.

ballast is higher than that in the bonding ballast. The larger the amount of glue used, the lower the elastic strain energy. The stiffness of the ballast bed is increased when ballast is bonded, which leads to the reduction of the elastic strain energy.

It is noticed the elastic strain energy of the conventional ballast shows obvious fluctuation during the cyclic loading process. On the contrary, it is more stable in the bonding ballast. It is caused by the fact that the spatial position of the ballast particles is more likely to be disturbed in the conventional ballast bed, causing the deformation of the ballast bed and aggravating the frictional energy dissipation. However, the ballast particles are constrained in the bonding ballast, and the spatial position of the ballast particles is more fixed. Therefore, the elastic strain energy becomes more stable and the frictional energy dissipation is less. As shown in Fig. 14, the frictional energy dissipation in the case of adding 33 kg/m^3 and 48 kg/m^3 glue is reduced to 22.8 % and 17% respectively after 100 loading cycles.

As shown in Fig. 15, the viscous strain energy in the bonding ballast decreases with the increase of the glue amount, which is similar to the change of the elastic strain energy. Besides, the viscous strain energy has a larger amplitude when adding more glue (48 kg/m^3) than that in the case of 33 kg/m^3 ballast glue. This can be related to the contact bonding strengthening and the amount of noncontact bonding increasing.

As shown in Fig. 16, the damping energy in the bonding ballast is higher than that in the conventional ballast. The damping energy in the conventional ballast can only be generated at the contact between ballast particles, while in the bonding ballast the glue plays a significant role in damping [26,37]. After 100 loading cycles, the damping energy in the case of 33 kg/m^3 and 48 kg/m^3 ballast glue is 1.9 and 2.9 times, respectively, that of the conventional ballast. The more glue is used, the stronger damping effect in the ballast is.

4.2.2. *Share ratio of different energy*

In order to further discover the behaviour of energy evolution, the energy ratio at the 1st, 5th, 10th, 25th, 50th, and 100th loading cycles are compared. The ratio of different energy is normalized according to the first peak value of elastic strain energy. The results are shown in Fig. 17-Fig. 19.

It can be seen from Fig. 17 that the frictional energy consumption is dominant in the initial loading stage (the 1st cycle), accounting for 56.3%, in the conventional ballast bed. Second to that is the elastic strain energy, accounting for 42.9%. The damping energy consumption can even be ignored which accounts for 0.8%. As the loading cycle increases, the proportion of elastic strain energy gradually increases and becomes the major, while that of frictional energy and damping energy gradually decreases. In the 100th loading cycle, the elastic strain energy accounts for 76.87%, the frictional energy and damping energy accounts for 22.96% and 0.17%, respectively. The change in the energy ratio reflects that the ballast is gradually compacted and becomes stable.

In the bonding ballast beds, the elastic strain energy has always been the major form as shown in Fig. 18 and Fig. 19. The elastic strain energy and frictional energy during loading in the bonding ballast beds show a similar trend as that in the conventional ballast bed. Differently, the viscous strain energy in the bonding ballast beds has a higher proportion. In the case of 33 kg/m^3 ballast glue, the proportion of frictional energy is in the second place at the beginning and gradually replaced

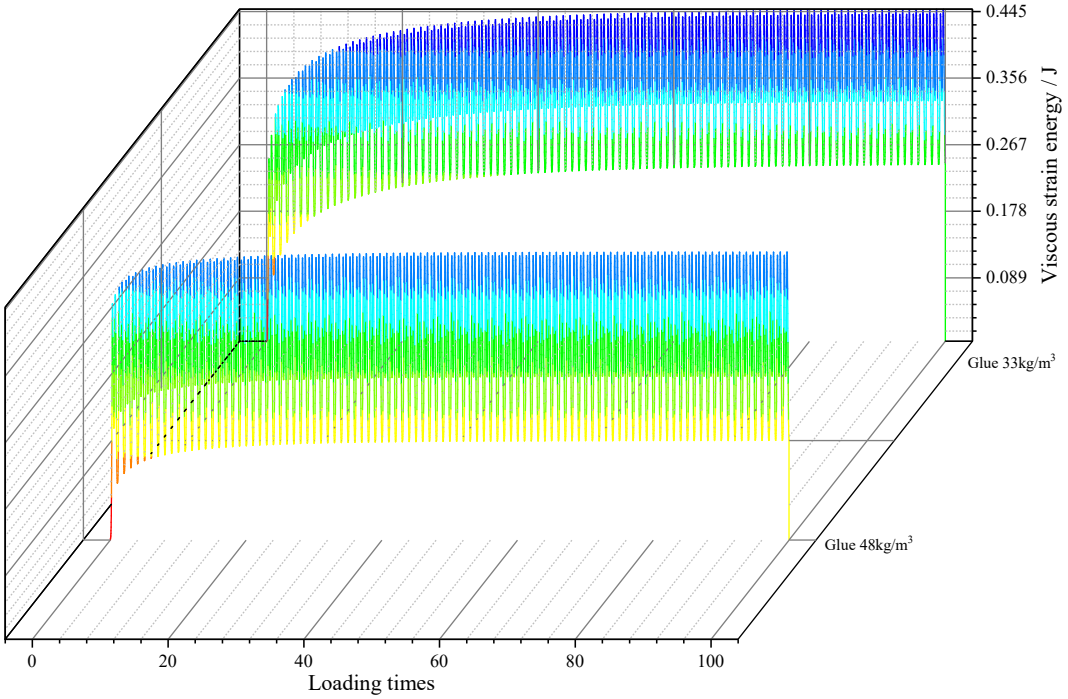

Fig. 15. Viscous strain energy evolution.

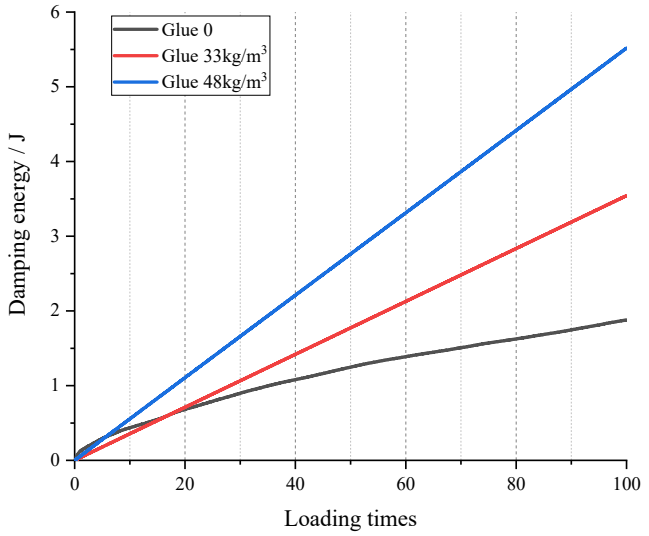

Fig. 16. Damping energy evolution.

viscous strain energy in the later cycles. On the contrary, the proportion of viscous strain energy in the case of 48 kg/m^3 ballast glue is always higher than that of frictional energy. The ratio of the elastic strain energy, viscous strain energy, frictional energy, and damping energy after 100 loading cycles is different in two cases of bonding ballast, which is 71.1%, 14.2%, 13.9%, 0.8% in the case of 33 kg/m^3 ballast glue and 66.2%, 20.5%, 11.8%, 1.5% in the case of 48 kg/m^3 ballast glue.

From the above analysis, it can be found that compared with the conventional ballast bed, the proportion of energy in the bonding ballast bed has changed significantly. The proportion of the elastic strain energy, viscous strain energy, and damping energy have increased, while that of the frictional energy is reduced. This change is larger when with a higher amount of glue.

4.3. Force and energy distribution at contact points

4.3.1. Contact points and contact force

There are complex states in the sleeper-ballast contact and the ballast-ballast contact in bonding ballast bed. In this section, the amount of sleeper-ballast contact and ballast-ballast contact is first counted and the contact forces at contact points are then analysed. After this, the energy at contact points is further studied.

The amounts of sleeper-ballast contact and ballast-ballast contact at

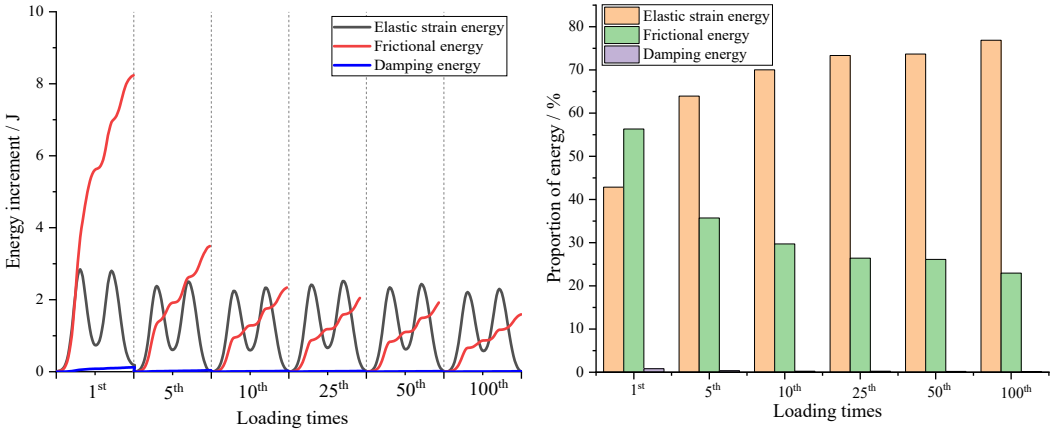

Fig. 17. Different energy in the conventional ballast bed: (a) Increment of energy dissipation; (b) Ratio.

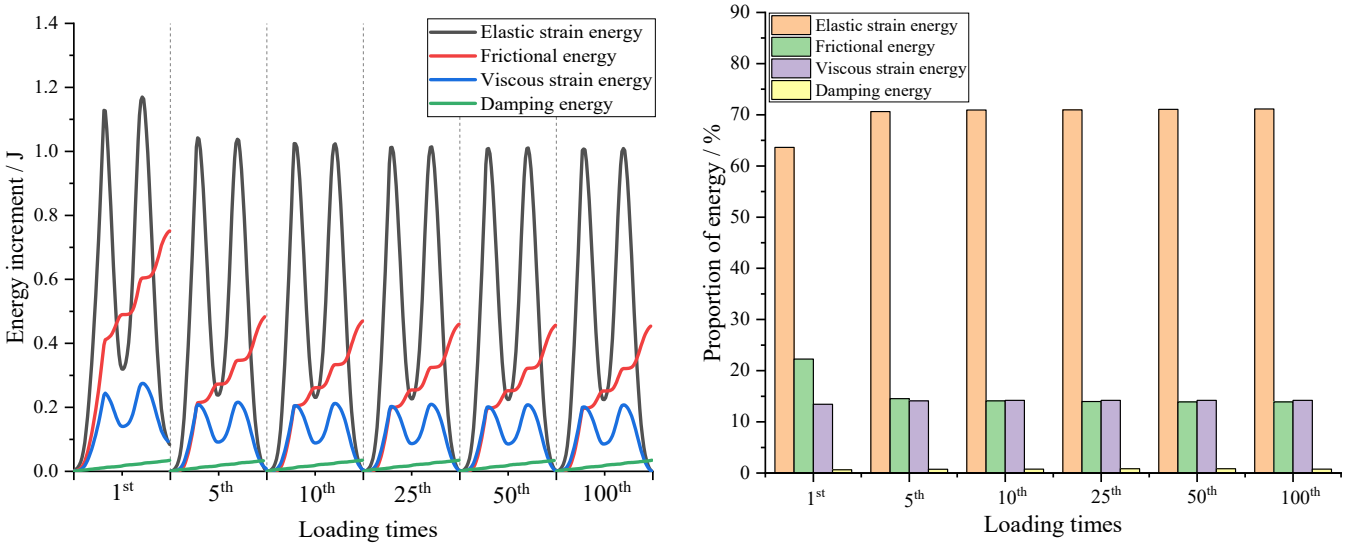

Fig. 18. Different energy in the bonding ballast bed 33 kg/m^3: (a) Increment of energy dissipation; (b) Ratio.

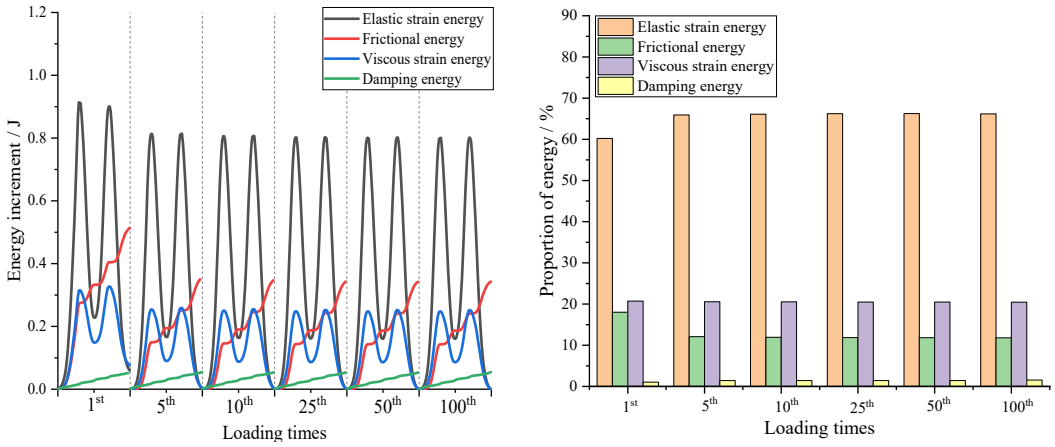

Fig. 19. Different energy in the bonding ballast bed 48 kg/m^3: (a) Increment of energy dissipation; (b) Ratio.

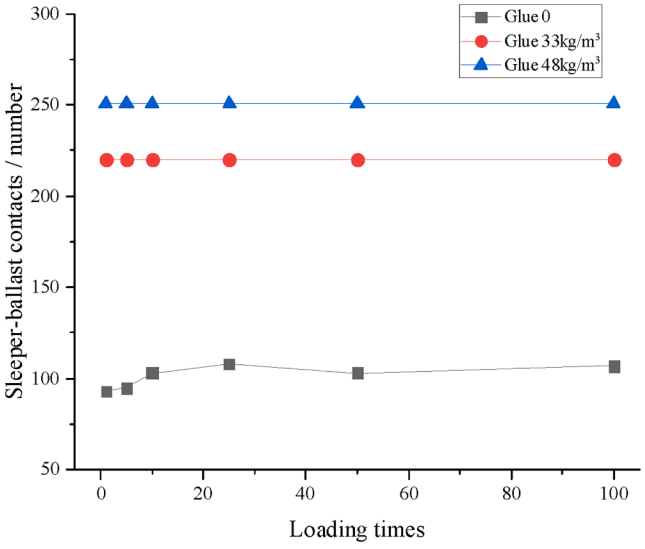

Fig. 20. Amount of the sleeper-ballast contact.

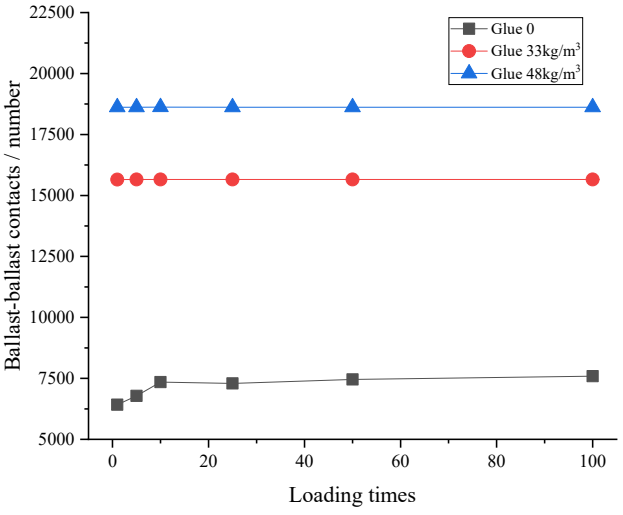

Fig. 21. Amount of the ballast-ballast contact.

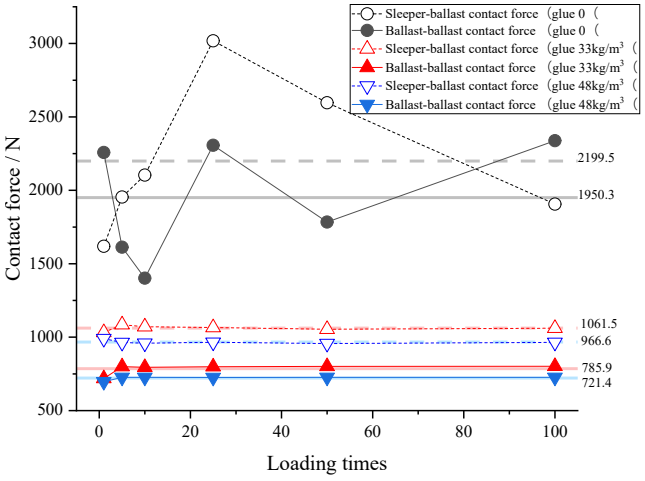

Fig. 22. Contact forces at various loading stages.

the 1st, 5th, 10th, 25th, 50th, and 100th loading cycles are compared in Fig. 20 and Fig. 21. It should be noted that due to the local refinement method, the amount of the Ballast-Sleeper Noncontact Bonding is increased by 7 times. To avoid this, the amount of sleeper-ballast contact before refinement is used here.

It can be seen from Fig. 20 and Fig. 21 that the amount of sleeper-ballast contact and ballast-ballast contact in the conventional ballast bed is the least. As the loading cycle increases, the amount of sleeper-ballast contact and ballast-ballast contact in the conventional ballast bed grows. This is because the ballast is gradually compacted during the load process. On the contrary, the amount of sleeper-ballast contact and ballast-ballast contact in the bonding ballast beds are considerably larger and increasing with the amount of ballast glue. Besides, the amount of contact points in the bonding ballast beds remains stable during the whole loading process, which shows good stability.

The statistics of the maximum contact forces at the 1st, 5th, 10th, 25th, 50th, and 100th loading cycles are shown in Fig. 22.

It can be seen from Fig. 22 that the maximum contact force of sleeper-ballast and ballast-ballast contacts in the conventional ballast bed is significantly higher than that of bonding ballast beds. Besides, the maximum contact forces of both contacts fluctuate largely during the loading process. The average maximum force of sleeper-ballast contact in the conventional ballast bed is larger than that of sleeper-ballast contact, which are 2199.5 N and 1950.3 N respectively. This confirms that the sleeper-ballast contact is the most crucial contact point. A similar trend can be found in the bonding ballast beds that the maximum

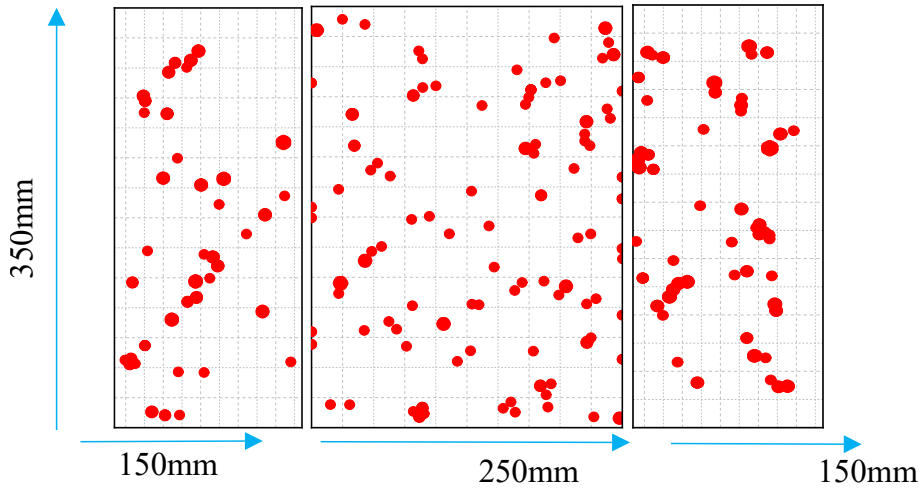

Fig. 23. Distribution of contact points in the conventional ballast bed: (a) Left, (b) Bottom, (c) Right.

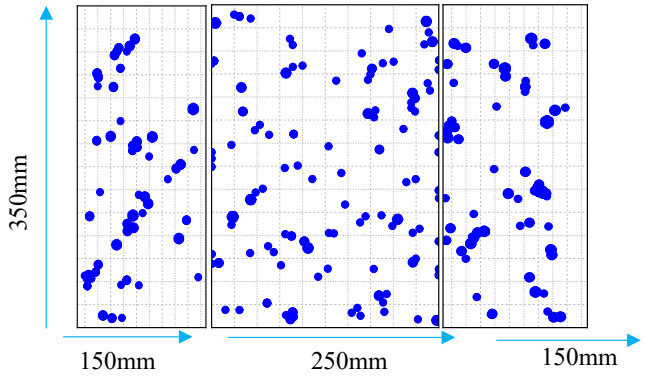

Fig. 24. Distribution of contact points in the bonding bed (glue 33 kg/m^3): (a) Left, (b) Bottom, (c) Right.

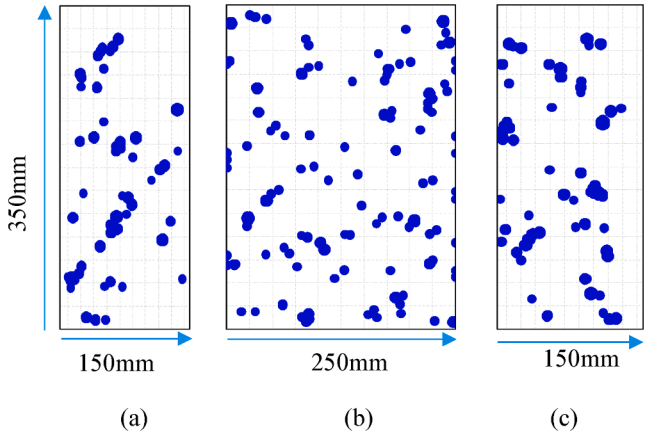

Fig. 25. Distribution of contact points in the bonding bed (glue 48 kg/m^3): (a) Left, (b) Bottom, (c) Right.

contact force of sleeper-ballast is also much larger than that ballast-ballast contacts, the average of which is 1061.5 N and 785.9 N respectively in the case of 33 kg/m^3 ballast glue and 966.6 N and 721.4 N respectively in the case of 48 kg/m^3 ballast glue. Here it can be found that the maximum contact forces are further reduced as more ballast glue is used, which is caused by the further increase of the contact points.

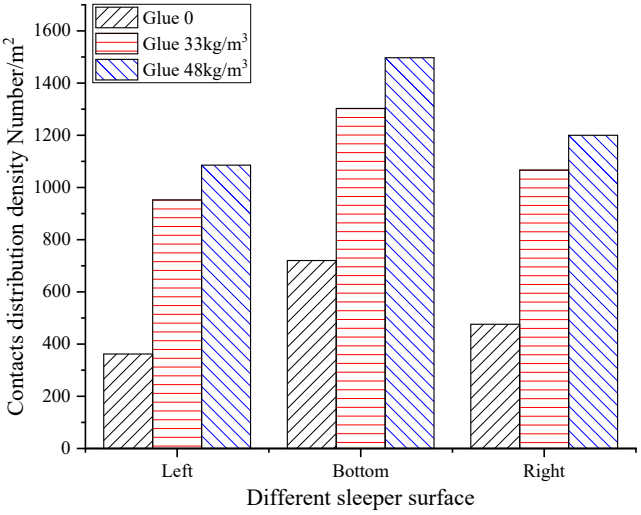

Fig. 26. Comparison of the distribution density of the contact points.

4.3.2. Distribution of sleeper-ballast contact points

From the above analysis, it can be found that the sleeper-ballast contact is the most critical contact area in the ballast bed, regardless of whether ballast glue is used or not. This section studies the distribution of different energy at sleeper-ballast contact points. Using the moment when the first peak in the 100th loading cycle of the train load is applied, the distribution of the contact points at the left, bottom, and right parts of the sleeper in the conventional ballast bed and bonding ballast beds are shown in Fig. 23-Fig. 25, wherein the location of the left, bottom, and right parts is indicated in Fig. 9.Fig. 24.

To see the changes in the amount of contact points, distribution density of the contact points at different parts is compared as shown in Fig. 26.

Fig. 26 shows that the density of the contact points at the bottom of the sleeper in the conventional ballast bed is 720 per m^2, and the average density of the contact points on the side of the sleeper is 419 per m^2. In the case of 33 kg/m^3 ballast glue is used, the density at the bottom is increased by 1.8 times and that at the side by 2.4 times. In the case of 48 kg/m^3 ballast glue, the increase of density is even more, which are 2.1 and 2.7 times for the bottom and side respectively. This shows that the density of the contact points increases significantly by bonding and the amount of ballast glue plays a positive role in increasing the density of the contact points. Besides, it can be also found that the density of the

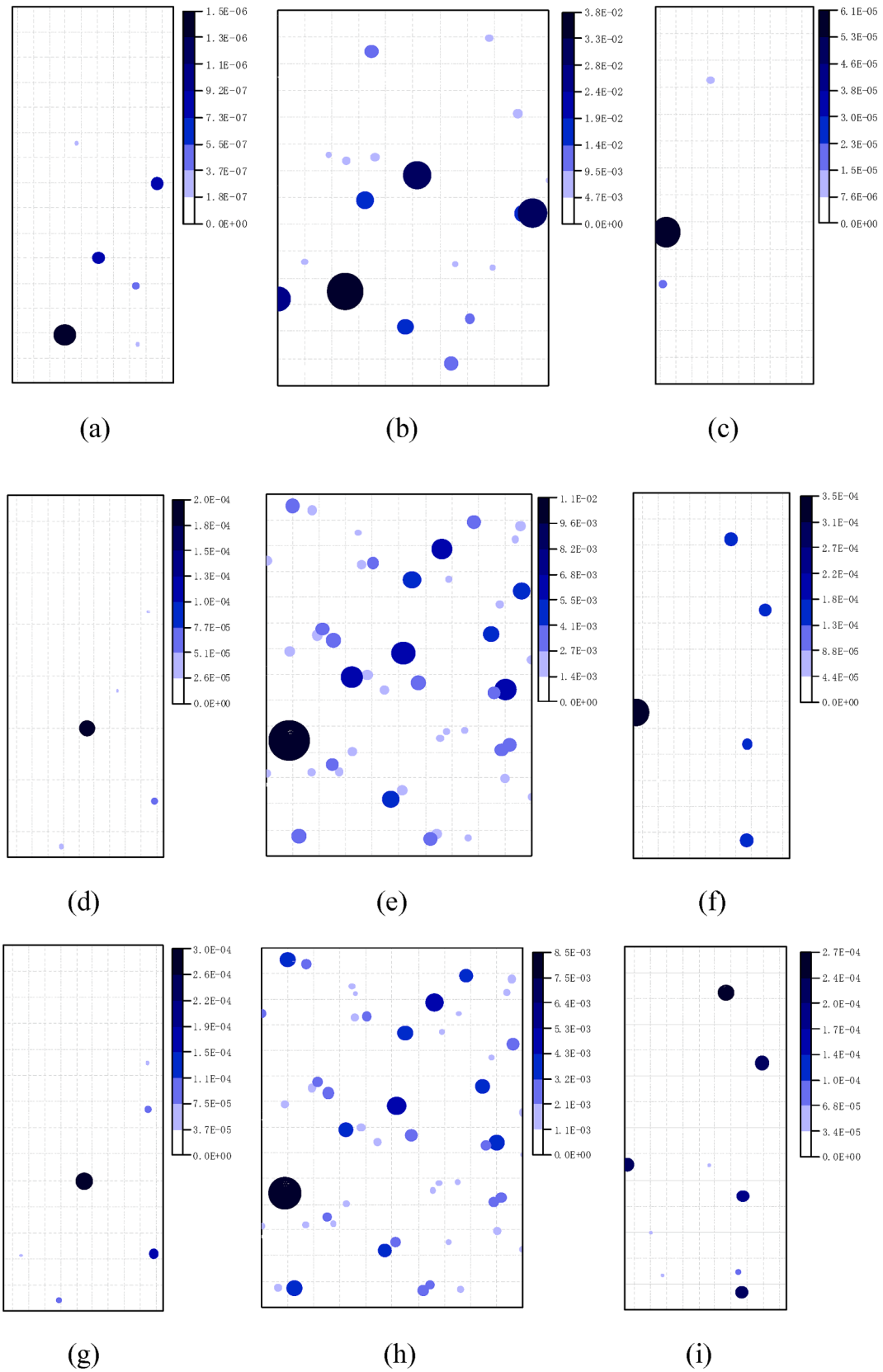

Fig. 27. Distribution of elastic strain energy (Unit J): (a) Left in the conventional ballast, (b) Bottom in the conventional ballast, (c) Right in the conventional ballast, (d) Left in the case of 33 kg/m^3, (e) Bottom in the case of 33 kg/m^3, (f) Right in the case of 33 kg/m^3, (g) Left in the case of 48 kg/m^3, (h) Bottom in the case of 48 kg/m^3, (i) Right in the case of 48 kg/m^3.

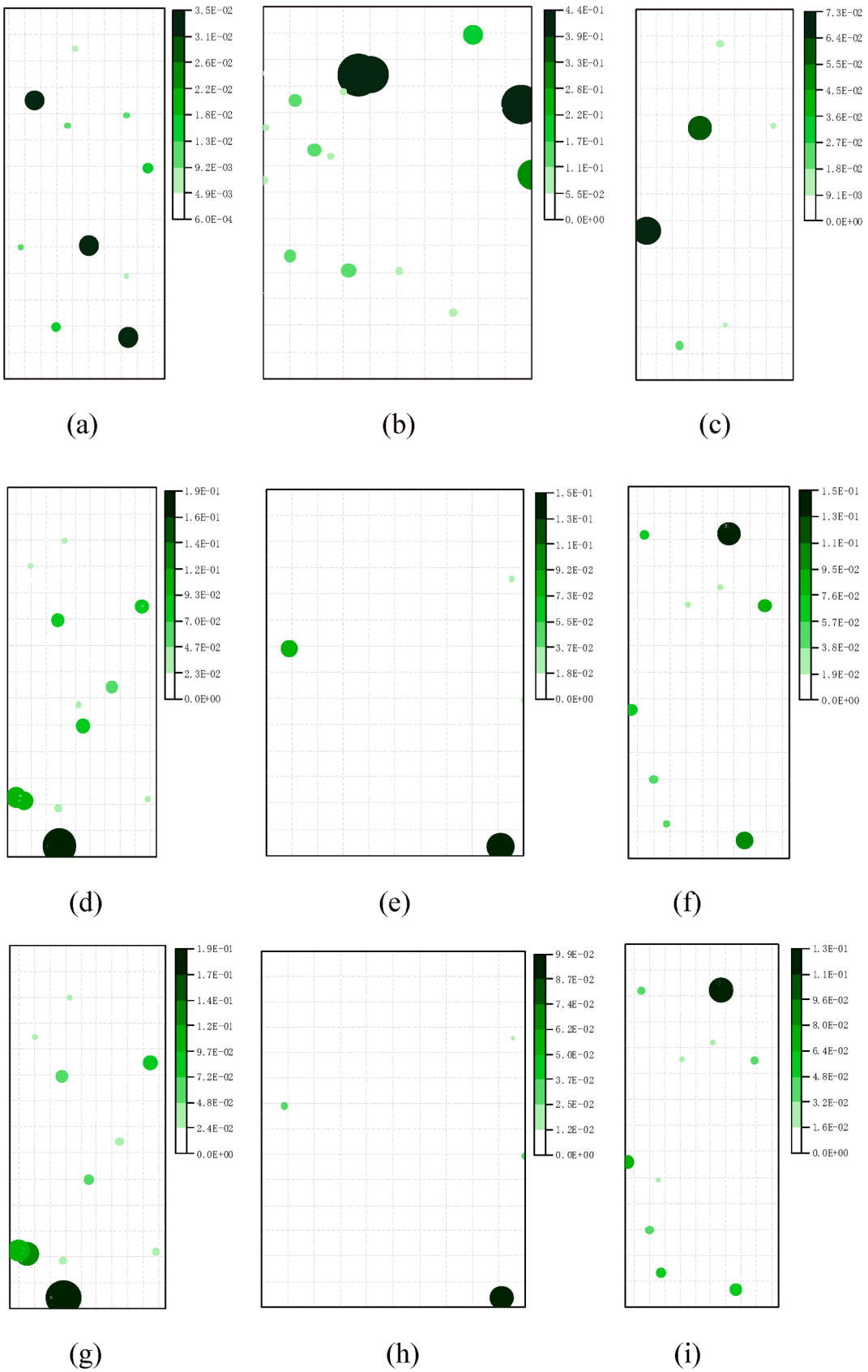

Fig. 28. Distribution of frictional energy (Unit J): (a) Left in the conventional ballast, (b) Bottom in the conventional ballast, (c) Right in the conventional ballast, (d) Left in the case of 33 kg/m^3, (e) Bottom in the case of 33 kg/m^3, (f) Right in the case of 33 kg/m^3, (g) Left in the case of 48 kg/m^3, (h) Bottom in the case of 48 kg/m^3, (i) Right in the case of 48 kg/m^3.

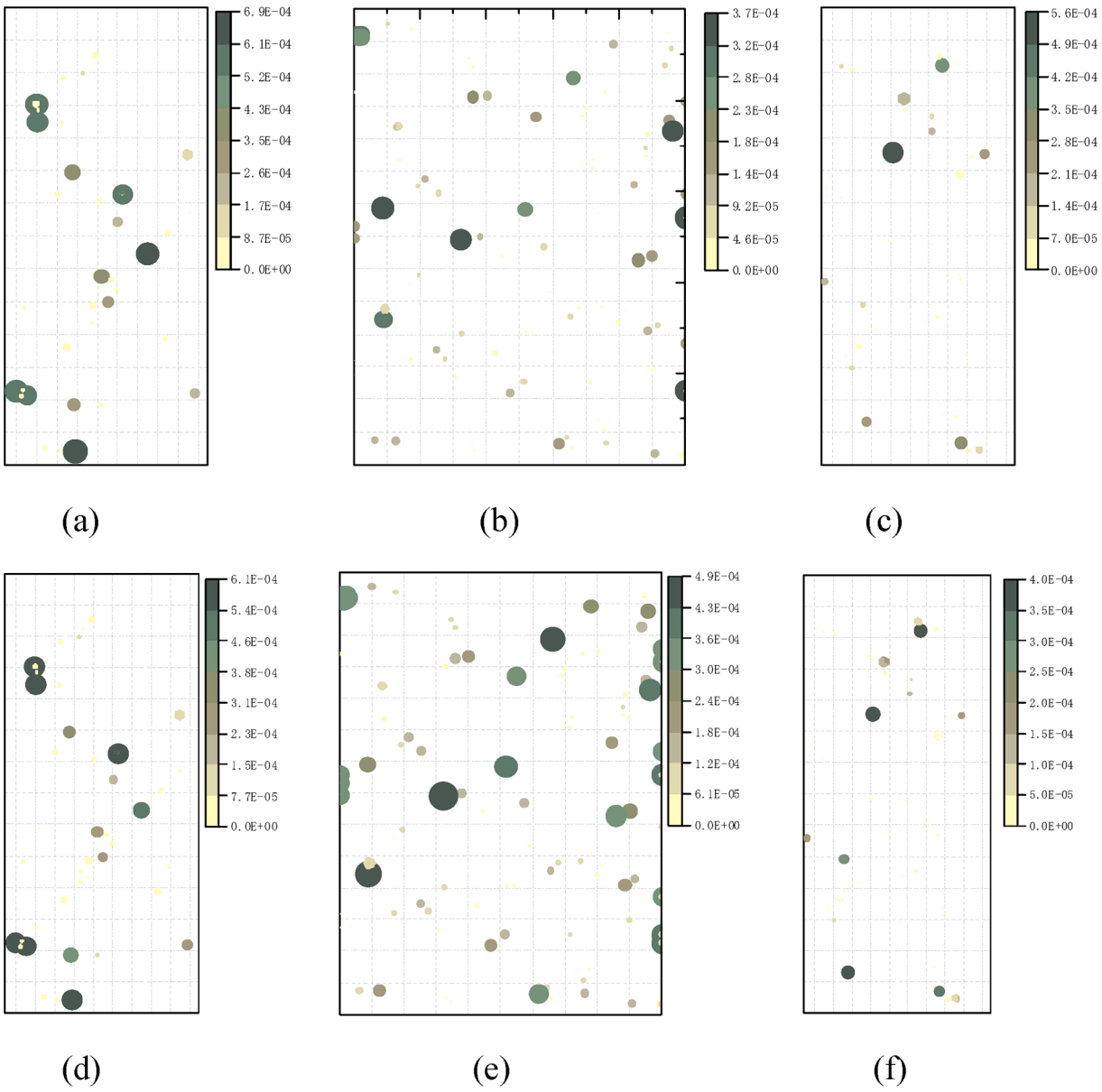

Fig. 29. Distribution of viscous strain energy (Unit J): (a) Left in the case of 33 kg/m^3, (b) Bottom in the case of 33 kg/m^3, (c) Right in the case of 33 kg/m^3, (d) Left in the case of 48 kg/m^3, (e) Bottom in the case of 48 kg/m^3, (f) Right in the case of 48 kg/m^3.

contact points at the bottom is much higher than that at the side in both conventional and bonding ballast beds, which indicates that the ballast particles at the bottom of the sleeper are in contact with the sleeper more sufficiently.

4.3.3. Energy at sleeper-ballast contact points

In this section, the distribution of elastic strain energy, frictional energy, viscous strain energy, and damping energy are analysed. The results are shown in Fig. 27-Fig. 30.

Fig. 27 shows that the elastic strain energy in the conventional ballast bed is mainly distributed at the bottom of the sleeper. The same trend can be also found in the bonding ballast beds, but the energy distributed to the side is more than that in the conventional ballast bed. Besides, the elastic strain energy is more evenly distributed in the bonding ballast beds. This is because the integrity of the ballast bed is improved after bonding.

Fig. 28 shows that the frictional energy in the conventional ballast bed is mainly distributed at the bottom of the sleeper as well. Although the frictional energy also appears at the side, its peak value is an order of magnitude smaller than that at the bottom. In the bonding ballast beds, the friction energy at the bottom is reduced while the friction energy at the side increases and eventually becomes the main position of friction energy distribution. This is because the ballast particles at the bottom of the sleeper move frequently in the conventional ballast bed and thus frictional energy at the bottom is relatively large. On the contrary, the sleeper and ballast particles are bonded as a whole in the bonding ballast beds so that the ballast particles are constrained, which makes the ballast particles at the bottom of the sleeper more stable when the sleeper moves vertically, while the large frictional energy is generated at the side due to large relative movement appearing between the sleeper and ballast particles.

Fig. 29 shows that the viscous strain energy has the same order of magnitude at the bottom and side of the sleeper in both cases of bonding ballast. The value of viscous strain energy is different according to the amount of ballast glue. This is because the viscous strain energy is dependent on the amount of bonding contact points, and using more ballast glue can generate more noncontact bonding contact points.

Fig. 30 shows that the damping energy in the bonding ballast beds is

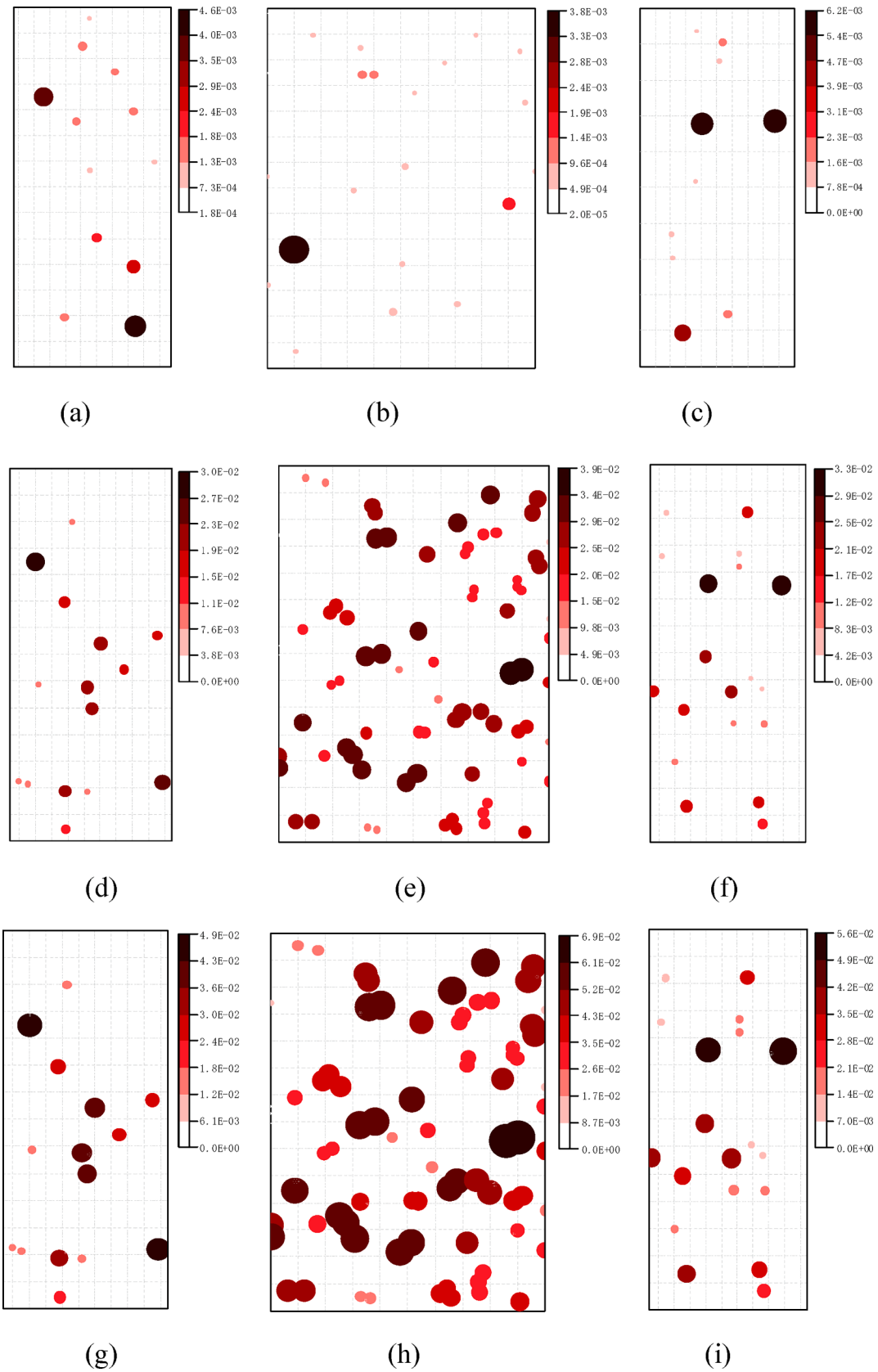

Fig. 30. Distribution of damping energy (Unit J): (a) Left in the conventional ballast, (b) Bottom in the conventional ballast, (c) Right in the conventional ballast, (d) Left in the case of 33 kg/m^3, (e) Bottom in the case of 33 kg/m^3, (f) Right in the case of 33 kg/m^3, (g) Left in the case of 48 kg/m^3, (h) Bottom in the case of 48 kg/m^3, (i) Right in the case of 48 kg/m^3.

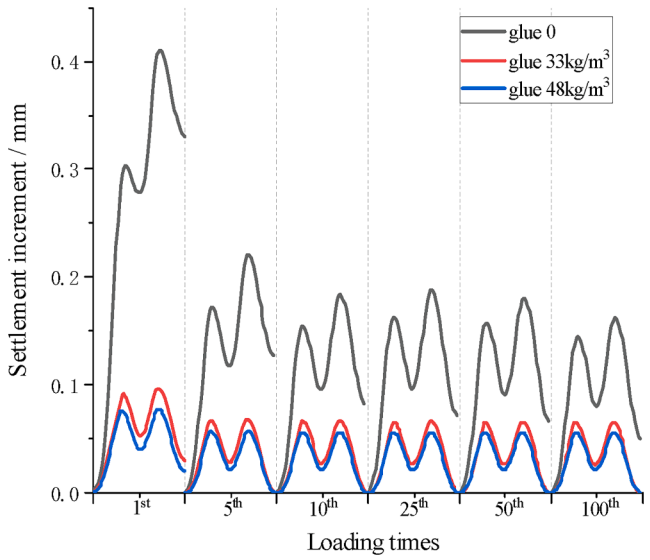

Fig. 31. Settlement increment at various loading stages.

by an order of magnitude larger than that in the conventional ballast bed and keeps increasing as the amount of ballast glue increases. It can be also seen that the damping energy at the bottom and the side are in the same order of magnitude in all cases. Improvement of the damping performance of the bonding ballast is caused by increase energy dissipation at contact points on the one hand, and the increase in the amount of contact points on the other hand.

4.4. Settlement and kinetic energy in ballast beds

4.4.1. Settlement in ballast beds

When a railway track is in the operational phase, ballast particles are constantly spatially rearranged under the cyclic loading of high-speed trains. Thus, the settlement of the ballast bed inevitably occurs. The section analysed the settlement behaviour by comparing the settlement in the conventional ballast and bonding ballast beds at various loading stages. The results are shown in Fig. 31.

It can be seen from Fig. 31 that the settlement increment in the conventional ballast bed and the bonding ballast beds are significantly different. For the conventional ballast bed, the settlement deformation during the loading process has a larger deformation in general. Besides, a large settlement increment remains after every loading cycle and, however, the remaining increment and amplitude of settlement flatten as the loading cycle grows, which indicates a process of compaction of the conventional ballast bed. On the contrary, the amplitude and increment of the settlement are both much smaller in the bonding ballast beds and the reduction is larger when more ballast glue is used. Besides, the amplitude and increment of settlement in the bonding ballast beds flatten much faster, meaning the bonding ballast beds become stabilised more quickly after loading while the conventional ballast bed still settles. Therefore, the bonding ballast bed can be used as a method for the rapid restoration of the railway track due to its excellent settlement behaviour.

4.4.2. Kinetic energy in ballast beds

The settlement in the ballast bed is a macroscopic phenomenon that is caused by the spatial motion of ballast particles in the complex stress state at the meso level. The more stable the ballast bed is, the stronger the spatial constraint of ballast particles have at the meso level and thus less easy to adjust their spatial position. Therefore, the section analyses the effect of ballast bonding on the moving behaviour of the ballast particles by comparing the spatial velocity distribution in both the conventional ballast and bonding ballast beds. The results of the velocity distribution in ballast beds at the first peak of the loading cycle are shown in Fig. 32.

Fig. 32 shows the ballast particles in the conventional ballast bed have a much larger velocity than that in the bonding ballast beds in all the presented loading cycles. The velocity of ballast particles further reduces when more ballast glue is added. A smaller velocity of ballast particles indicates the ballast particles are more stable under the impact of train loads.

From the energy point of view, under the same impact of train load, the smaller the spatial velocity of the ballast particles leads to the lower kinetic energy of the ballast particles and, thus, the lower kinetic energy of the ballast bed. To further analysis, the time history curves of the kinetic energy of the conventional and bonding ballast beds are compared in Fig. 33.

It can be seen from Fig. 33 that the kinetic energy of the convention ballast bed at various loading stages is always significantly higher than that of the bonding ballast bed, and the fluctuation patterns of the kinetic energy are different at each loading stage. Besides, the kinetic energy in the conventional ballast bed shows a decreasing trend as the loading cycle increases. On the contrary, the kinetic energy of the bonding ballast beds lower and the kinetic energy fluctuates in the same pattern after the first loading cycle. This is because the constraint of the ballast particles in the conventional ballast bed is in an unstable state, which leads to higher kinetic energy in the ballast bed and different fluctuation patterns at each loading stage, meaning the mode of the spatial migration of ballast particles has greater uncertainty. For the bonding ballast, the constraint of the ballast particles is more stable. As a result, the mode of the spatial migration of ballast particles is relatively certain and, therefore, the kinetic energy in the ballast bed is smaller and the fluctuation patterns at different loading stages are similar, which makes the settlement of bonding ballast beds convergences more quickly.

5. Conclusions

Comparing to the conventional ballast bed, the mechanical behaviour of bonding ballast beds is significantly changed. The most important reason is the changes in the contact between ballast particles. The mechanical behaviour at the sleeper-ballast contact and the ballast-ballast contact in the bonding ballast are complex and, thus, developing proper constitutive models to analyse various types of bonding contacts at the *meso*-level is crucial. Besides, because the essence of the change in the mechanical behaviour lies in the process of storage and dissipation energy, this paper uses the discrete element method to study the constitutive model of and energy dissipation in the bonding ballast bed. The main conclusions are as follows.

(1) The defects of the parallel bond model that commonly used for the simulation of bonding ballast are studied, which are: (a) the amount of bonding contact shoulde be increased as the amount of ballast glue increasing; (b) the state of ballast bed, such as gradation and compactness, is not considered; (c) the bonding force between ballast particles at the *meso*-level does not have a clear physical meaning. To overcome the defects, the parallel bond model is revised. Four kinds of bonding contacts are provided including Ballast-Ballast Contact Bonding, Ballast-Ballast Noncontact Bonding, Ballast-Sleeper Contact Bonding, and Ballast-Sleeper Noncontact Bonding.

(2) The evolution forms of main energy in the conventional and bonding ballast beds under the cyclic loading of high-speed trains are different. In the conventional ballast bed, the frictional energy is the main form in the initial stage of loading and later replaced by the elastic strain energy. On the contrary, the elastic strain energy has always been the main dissipation form in the bonding ballast bed, followed by viscous strain energy, frictional energy, and damping energy.

(3) Compared with the conventional ballast bed, there is more contacts in the bonding ballast bed and the amount of contacts is further increased when more ballast glue is used. The sleeper-ballast contact is

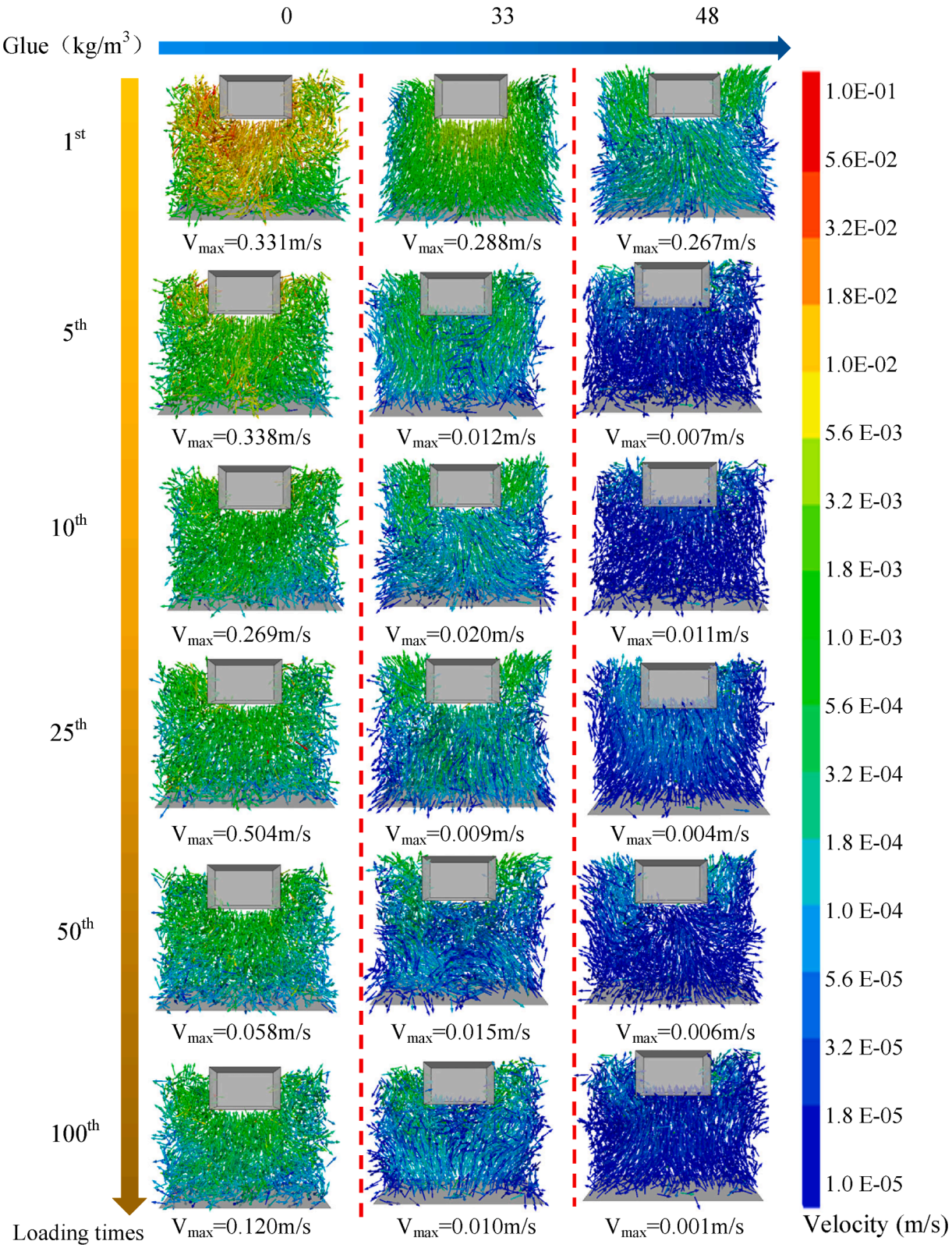

Fig. 32. Velocity distribution in ballast beds.

the most critical contact area in the ballast bed. After bonding, the amount of contacts is significantly increased at the bottom and sides of the sleeper and all forms of energy become more evenly distributed at both the bottom and sides of the sleeper.

(4) The settlement of the bonding ballast bed under cyclic loading is related to the kinetic energy of the ballast particles at the *meso*-level. At the meso level, the kinetic energy of the bonding ballast fluctuates with smaller amplitude and convergences more quickly under cyclic loading, which is reflected in the macroscopic aspect that the settlement of the bonding ballast bed is relatively small and can be fast completed.

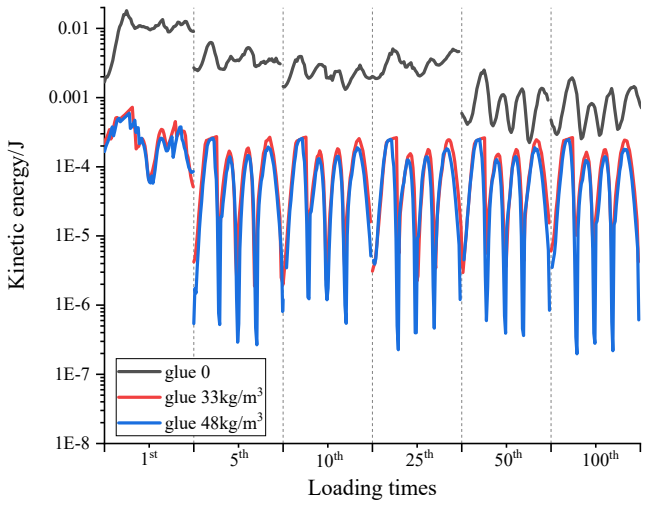

Fig. 33. Time history curves of the kinetic energy of ballast beds.

CRediT authorship contribution statement

Hong Xiao: Conceptualization, Funding acquisition, Project administration, Formal analysis, Writing – original draft. **Xing Ling:** Formal analysis, Software, Validation, Writing – original draft, Writing – review & editing. **Meng Wang:** Investigation, Supervision, Validation. **Shu-Wei Fang:** Investigation, Methodology, Resources. **Hao-Yu Wang:** Supervision, Validation, Writing – review & editing.

Declaration of Competing Interest

The authors declare that they have no known competing financial interests or personal relationships that could have appeared to influence the work reported in this paper.

Acknowledgments

This work was supported by the National Natural Science Foundation of China (No. 51578055)

Appendix

Research on polyurethane-mixed ballast.

Authors	Affiliation	Year	Research Content	Research Method
P K Woodward et al. [11–12]	Heriot-Watt University	2007, 2010	Compared the acceleration of track with and without bonding ballast. Results show that polyurethane-mixed ballast can reduce the vibration of sleepers.	Field tests of vibration acceleration
S Kaewunruen [13]	Massachusetts Institute of Technology	2014	Studied the vibration characteristics of rails and sleepers before and after bonding ballast. Results show that the high-frequency noise between the wheel and rail is increased after ballast bonding, while the vibration of the sleeper and ballast is suppressed.	Field tests of vibration acceleration
C Zhao et al. [4]	Southwest Jiaotong University	2015	Studied the mechanical behaviour of the transition zone between ballast track and slab track after using ballast bonding and auxiliary rails. Results show that ballast bonding and auxiliary rails smoothen the stiffness in the track transition and consequently improve the vehicle-track dynamic response.	Field tests of vertical static track stiffness and vibration acceleration
L Qie et al. [2]	China Academy of Railway Sciences	2015	Using a track loading vehicle tested the lateral resistance track and vertical displacement of rails of the track with and without bonding ballast. The results show that the track with bonding ballast has better resistance to lateral deformation and the force on sleepers at different location are distributed more evenly.	Field tests of lateral resistance and vertical displacement
A Kruglikov et al. [14]	Rostov State Transport University	2017	Studied Young's modulus and lateral resistance of the ballast after the ballast particles on the shoulder were bonded. Results show that Young's modulus and lateral resistance of bonded ballast are significantly improved. Besides, the ground penetrating radar (GPR) can detect the depth of ballast bonding.	Field tests of lateral resistance
W Qi et al. [3]	Southwest Jiaotong University	2018	Tested the dynamic behaviour of a track transition zone in a heavy-haul railway with partial bonding ballast and full-section bonding ballast. The results show that the displacement and acceleration of rails and sleepers can be gradually changed after varying the mode of bonding ballast.	Field tests of track dynamic behaviour
H Xiao et al. [15–16]	Beijing Jiaotong University	2017, 2019	Tested the lateral resistance and support stiffness of the track with ballast bonding. The results show that lateral resistance and support stiffness of the track is significantly increased and can be continuously increased if adding more ballast glue.	Field tests of lateral resistance and support stiffness
S Yang et al. [17]	Jinan–Qingdao high-speed railway Co.	2019	Tested the vibration characteristics of the track with ballast bonding and the wind field distribution on the surface. The results show that the track with ballast bonding has a better damping effect on high-frequency vibration.	Field tests of track dynamic behaviour
J Xiao et al. [10]	Southwest Jiaotong University	2020	Studied the effect of ballast bonding on the performance of high-speed railway tracks in subgrade fracture zone using a	Field tests of track geometric state

(*continued on next page*)

(*continued*)

Authors	Affiliation	Year	Research Content	Research Method
			year-long monitoring data set. The results show that the track quality index of the tested track slightly exceeds the limit in the standard, but it can be improved by adjusting fasteners.	
P K Woodward et al. [18–21]	Heriot-Watt University	2009–2014	Studied the stiffness change and deformation behaviour of bonded ballast under cyclic loading using a full-scale model. The results show that ballast bonding can significantly increase the stiffness and reduce the deformation of ballast. The bonded ballast has good drainage but the initial moisture content in the ballast affects the bonding effect.	Laboratory tests of full-scale ballast box model(Geopavement and Railways Accelerated Fatigue Testing)
M S Dersch et al. [22]	University of Illinois at Urbana-Champaign	2010	Conducted shear tests on the bonded ballast specimens and studied the shear resistance after different bonding days. The results show that the longer the bonding time, the higher the strength of the specimens. In addition, the bonded ballast is higher resistance to breakage, and thus the ballast particles are more stable.	Laboratory tests of direct shear strength
A Keene et al. [23]	University of Texas at Austin	2014	Conducted bending tests, compression tests (unconfined) and cyclic triaxial loading tests on bonded ballast specimens. The results show that the bending resistance of bonded ballast is similar to that of cement-stabilized soil; its elastic modulus and compressive strength are both lower than that of cement-stabilized soil; it has less cumulative plastic deformation than clean and dirty ballasts.	Laboratory tests of compression and bending, triaxial loading
L Qie et al. [2]	China Academy of Railway Sciences	2015	Conducted fatigue tests and freeze–thaw tests on bonded ballast specimens. The results show that the bonded ballast has good elasticity and resistance to accumulative settlement under the cyclic loads.	Laboratory tests of fatigue and freeze–thaw cycle
S H Lee et al. [24]	Korea Railroad Research Institute	2017	Studied the effect of the amount of ballast glue on the stiffness and strength of bonded ballast specimens. Results show that both the stiffness and strength of bonded ballast increase with the amount of ballast glue. The bonded ballast specimens with a low amount of ballast glue may crack under loading.	Laboratory tests of large-scale triaxial loading
R F du Plooy et al. [25]	University of Pretoria	2017	Studied the settlement characteristics of the track with bonding ballast under cyclic heavy-haul train loads using a full-scale model. The results show that bonding ballast can significantly reduce track settlement and thus is helpful to keep track geometry and reduce maintenance cost.	Laboratory tests of cyclic loading box
G D'Angelo et al. [26–28]	The University of Nottingham	2016–2018	Conducted uniaxial loading tests and box tests to study the deformation behaviour of the bonding ballast. The results show that the deformation of bonded ballast is significantly reduced due to changes in stiffness and energy dissipation. In addition, conventional track maintenance including tamping, stone blowing can also be used on the track with bonding ballast.	Laboratory tests of uniaxial loading and ballast box loading
G Jing et al. [5,29]	Beijing Jiaotong University	2019	Studied the lateral resistance of the track with various bonding methods using a full-scale model. The results show that the bonding under the centre of sleepers, under two ends of sleepers and the whole area of sleepers can all significantly increase the lateral resistance of track.	Laboratory tests of lateral resistance
M Esmaeili et al. [30]	Iran University of Science and Technology	2020	Studied the effect of glue composition and bonding methods on the deformation behaviour of the track with ballast bonding. The results show that the asphalt-cement ratio of 0.42 achieves the best effect when considering the settlement, stiffness, and damping behaviour of the ballast in case of the bottom of the ballast is bonded.	Laboratory tests of ballast box
D Gundavaram and S Hussaini [31]	Indian Institute of Technology Patna	2020	Conducted the shear test on the bonded ballast specimens under various normal stress and shear rates. The results show that the bonded ballast can significantly improve the shear strength. The friction angle and expansion angle of the bonded ballast is increased. As normal stress and shear rate growing, the crushing rate of particles of unbonded ballast has increased while the particles in the bonded ballast have not been crushed.	Laboratory tests of direct shear
D M Barbieri et al. [32]	Norwegian University of Science and Technology	2020	Compared the effect of the various ballast glue including bitumen, polyurethane, organosilane, and lignosulphonate and found that they all have a significant effect on elastic modulus and resistance to plastic deformation.	Laboratory tests of repeated triaxial loading
P K Woodward et al. [61–63]	Heriot-Watt University	2009–2014	Compared the dynamic behaviour of the track with and without ballast bonding and analysed the changes in resistance using the FEM method. The results showed that the track with ballast bonding has better resistance to deformation and the later resistance is significantly improved.	FEM simulations of static and dynamic track response
S Thomas et al. [33]	Heriot-Watt University	2015	Developed a track-bridge model using the FEM method and analysed the stress changes of the bridge after using the ballast bonding. The results show that the use of ballast bonding can improve the distribution of the train load and reduce the stress of the bridge.	FEM simulations of a arch railway bridge
X Cai et al. [34]	Beijing Jiaotong University	2019	Combined the FEM method with multi-body dynamics theory to analyse the mechanical behaviour of the track in the tunnel	FEM simulations of vehicle–track–tunnel system

(*continued on next page*)

(*continued*)

Authors	Affiliation	Year	Research Content	Research Method
			of heavy-haul railways when the ballast foam bonding is used. The results show that the track with ballast bonding has lower track stiffness and vibration of the tunnel.	
G Jing et al. [5,35]	Beijing Jiaotong University	2012, 2019	Developed a DEM mode for a box test to analyse the *meso*-mechanical behaviour of ballast bonding. The results show that the displacement of the ballast particles was reduced due to the bonding effect and the maximum contact force in the ballast reduces as the depth of bonding growing.	DEM simulations of sleeper-ballast structure
Y Xu et al. [36]	China Academy of Railway Sciences	2019	Studied the accumulative settlement and contact force distribution in bonded ballast using the DEM method. The results show that the ballast bonding can reduce the residual deformation of the ballast and effectively reduce the dynamic stress in the ballast.	DEM simulations of ballast box
H Xiao et al. [1,15,16,37,38]	Beijing Jiaotong University	2017–2020	Developed the 3 sleepers-ballast model, ballast box test model and triaxial loading model to analyse the later and vertical mechanical behaviours of bonded ballast. The results show that later and vertical mechanical behaviour, energy dissipation, deformation behaviour of the bonded ballast is changed significantly.	DEM simulations of sleepers-ballast structure and ballast box, triaxial loading

References

[1] X. Ling, H. Xiao, G. Liu, M. Zhang, Discrete element modeling of polyurethane-stabilized ballast under monotonic and cyclic triaxial loading [J], Constr. Build. Mater. 255 (2020) 119370, https://doi.org/10.1016/j.conbuildmat.2020.119370.

[2] L. Qie, H. Wang, Y. Xu, et al., Experimental study on mechanical performance of polyurethane solidified ballast bed [J], Railway Engineering 1 (2015) 107–112. In Chinese.

[3] W. Qi, Y. Liu, C. Li, Dynamic testing and analysis of ballasted track of different stiffness sections using polyurethane ballast reinforcement technique[J], Journal of Central South University (Science and Technology) 49 (3) (2018) 764–770. In Chinese.

[4] C. Zhao, P. Wang, Q. Yi, D. Meng, Application of polyurethane polymer and assistant rails to settling the abnormal vehicle-track dynamic effects in transition zone between ballastless and ballasted track[J], Shock Vib. 2015 (2015) 1–9.

[5] G. Jing, X.u. Zhang, W. Jia, Lateral resistance of polyurethane-reinforced ballast with the application of new bonding schemes: Laboratory tests and discrete element simulations [J], Constr. Build. Mater. 221 (2019) 627–636.

[6] G. Jing, W. Jia, H. Fu, et al., Research on the Availability of Special Polyurethane for High-speed Railway Ballast Flight Prevention [J], Journal of railway engineering society 36 (05) (2019) 25–29. In Chinese.

[7] S. Lakušic, M. Ahac, I. Haladin, Track stability using ballast bonding method[C]// 10th Slovenian, Road and Ttransportation Congress. (2010).

[8] G. Jing, L. Qie, V. Markine, W. Jia, Polyurethane reinforced ballasted track: Review, innovation and challenge [J], Constr. Build. Mater. 208 (2019) 734–748.

[9] P.K. Woodward, A. El Kacimi, O. Laghrouche, G. Medero, M. Banimahd, Application of polyurethane geocomposites to help maintain track geometry for high-speed ballasted railway tracks [J], Journal of Zhejiang University SCIENCE A 13 (11) (2012) 836–849.

[10] J.-L. Xiao, P.u. Jing, S.-X. Yu, P. Wang, Analysis on the track quality evolution law of polyurethane-reinforced ballasted track in high-speed railway [J], Proceedings of the Institution of Mechanical Engineers, Part F: Journal of Rail and Rapid Transit 235 (8) (2021) 993–1005.

[11] Woodward P K, Thompson D, Banimahd M. Geocomposite technology: reducing railway maintenance[C]// Proceedings of the Institution of Civil Engineers-Transport. Thomas Telford Ltd, 2007, 160(3): 109-115.

[12] Woodward P K, Kennedy J, Medero G. Improving the safety of the railway track infrastructure using insitu polyurethane geocomposites[C]//2010 AREMA Annual Meeting, Number AREMA, Orlando, FL. 2010.

[13] Kaewunruen S. Dynamic responses of railway bridge ends: A systems performance improvement by application of ballast glue/bond[C]//Proceedings of the Second International Conference on Railway Technology: Research, Development and Maintenance, Ajaccio, Corsica, France. 2014.

[14] A.A. Kruglikov, V.A. Yavna, Y.M. Ermolov, A.G. Kochur, Z.B. Khakiev, Strengthening of the railway ballast section shoulder with two-component polymeric binders[J], Transp. Geotech. 11 (2017) 133–143.

[15] H. Xiao, X. Ling, Experiment and DEM Analysis of Lateral Resistance of Glued Ballast [J], Journal of Southwest Jiaotong University 52 (6) (2017) 1046–1054. In Chinese.

[16] X. Ling, H. Xiao, Experimental study and discrete element analysis on mechanical properties of glued ballast with different glue consumption [J], Journal of the China railway society 41 (10) (2019) 107–114. In Chinese.

[17] S. Yang, Q. Chai, H. Jiang, et al., Test and Analysis of Dynamic Characteristics of Polyurethane Curing Track Bed for Jinan-Qingdao High Speed Railway [J], Railway engineering 59 (11) (2019) 101–104. In Chinese.

[18] P.K. Woodward, J.H. Kennedy, G.M. Medero, XiTRACK reinforcement of high speed railway track over peat formations[C]//10th International Railway Engineering Conference, University of Westminster, London, 2009.

[19] P.K. Woodward, J. Kennedy, G.M. Medero, M. Banimahd, Maintaining absolute clearances in ballasted railway tracks using in situ three-dimensional polyurethane geocomposites[J], Proceedings of the Institution of Mechanical Engineers, Part F: Journal of Rail and Rapid Transit 226 (3) (2012) 257–271.

[20] P.K. Woodward, J. Kennedy, O. Laghrouche, D.P. Connolly, G. Medero, Study of railway track stiffness modification by polyurethane reinforcement of the ballast [J], Transp. Geotech. 1 (4) (2014) 214–224.

[21] J. Kennedy, P.K. Woodward, G. Medero, M. Banimahd, Reducing railway track settlement using three-dimensional polyurethane polymer reinforcement of the ballast[J], Constr. Build. Mater. 44 (2013) 615–625.

[22] M.S. Dersch, E. Tutumluer, C.T. Peeler, et al., Polyurethane coating of railroad ballast aggregate for improved performance[C]//Joint Rail, Conference. 49064 (2010) 337–342.

[23] A. Keene, J.M. Tinjum, T.B. Edil, Mechanical properties of polyurethane-stabilized ballast[J], Geotechnical engineering journal 45 (1) (2014) 66–73.

[24] S.H. Lee, S.J. Lee, J.G. Park, Y.-T. Choi, An experimental study on the characteristics of polyurethane-mixed coarse aggregates by large-scale triaxial test [J], Constr. Build. Mater. 145 (2017) 117–125.

[25] R.F.D. Plooy, P.J. Graebe, Characterisation of rigid polyurethane foam reinforced ballast through cyclic loading box tests[J], Journal of the South African Institution of Civil Engineers 59 (2017) 2–10.

[26] G. D'Angelo, N. Thom, D. Lo Presti, Bitumen stabilized ballast: A potential solution for railway track-bed[J], Constr. Build. Mater. 124 (2016) 118–126.

[27] G. D'Angelo, D. Lo Presti, N. Thom, Optimisation of bitumen emulsion properties for ballast stabilisation[J], Materiales de Construcción 7 (080) (2017) 124, https://doi.org/10.3989/mc.1957.v07.i08010.3989/mc.2017.04416.

[28] G. d'Angelo, M. Sol-Sánchez, F. Moreno-Navarro, D. Lo Presti, N. Thom, Use of bitumen-stabilised ballast for improving railway trackbed conventional maintenance[J], Géotechnique 68 (6) (2018) 518–527.

[29] G. Jing, W. Jia, H. Fu, et al., High-Speed Ballasted Railway Track Lateral Resistance Characteristics and Reinforcements [J], Journal of Southwest Jiaotong University 54 (5) (2019) 1087–1092. In Chinese.

[30] M. Esmaeili, M. Paricheh, M.H. Esfahani, Laboratory investigation on the behavior of ballast stabilized with bitumen-cement mortar[J], Constr. Build. Mater. 245 (2020) 118389, https://doi.org/10.1016/j.conbuildmat.2020.118389.

[31] D. Gundavaram, S.K.K. Hussaini, Performance evaluation of polyurethane-stabilized railroad ballast under direct shear conditions[J], Constr. Build. Mater. 255 (2020) 119304, https://doi.org/10.1016/j.conbuildmat.2020.119304.

[32] D.M. Barbieri, M. Tangerås, E. Kassa, I. Hoff, Z. Liu, F. Wang, Railway ballast stabilising agents: Comparison of mechanical properties[J], Constr. Build. Mater. 252 (2020) 119041, https://doi.org/10.1016/j.conbuildmat.2020.119041.

[33] S. Thomas, P. Woodward, O. Laghrouche, Influence of stiffening ballasted track bed overlying a masonry arch bridge using a polyurethane polymer material[J], Constr. Build. Mater. 92 (2015) 111–117.

[34] X. Cai, Y. Zhong, X. Hao, Y. Zhang, R. Cui, Dynamic behavior of a polyurethane foam solidified ballasted track in a heavy haul railway tunnel[J], Adv. Struct. Eng. 22 (3) (2019) 751–764.

[35] G.Q. Jing, L. Shao, Y.D. Zhu, L. Gao, Micro-analysis of railway ballast bond effects [C]//Advanced Materials Research, Trans Tech Publications Ltd 446-449 (2012) 2492–2496.

[36] Y. Xu, L. Qie, H. Wang, Mechanical properties of polyurethane ballast bed based on discrete element method [J], Journal of Tongji University (NATURAL SCIENCE) 47 (8) (2019) 1156–1161. In Chinese.

[37] X. Ling, H. Xiao, X. Cui, Analysis of mechanical properties of polyurethane-mixed ballast based on energy method [J], Constr. Build. Mater. 182 (2018) 10–19.

[38] X. Ling, H. Xiao, F. Jin, Investigating the effect of different bonding areas on the lateral resistance of polyurethane-mixed ballast using the discrete element method, Proceedings of the Institution of Mechanical Engineers, Part F: Journal of Rail and Rapid Transit 235 (2) (2021) 133–142.
[39] User's Guide. Minneapolis. (2015).
[40] Y. Guo, H. Fu, Y.u. Qian, V. Markine, G. Jing, Effect of sleeper bottom texture on lateral resistance with discrete element modelling[J], Constr. Build. Mater. 250 (2020) 118770, https://doi.org/10.1016/j.conbuildmat.2020.118770.
[41] S. Shi, L. Gao, X. Cai, H. Yin, X. Wang, Effect of tamping operation on mechanical qualities of ballast bed based on DEM-MBD coupling method[J], Comput. Geotech. 124 (2020) 103574, https://doi.org/10.1016/j.compgeo.2020.103574.
[42] Z. Shen, M. Jiang, C. Thornton, DEM simulation of bonded granular material. Part I: contact model and application to cemented sand[J], Comput. Geotech. 75 (2016) 192–209.
[43] M. Lu, G.R. McDowell, The importance of modelling ballast particle shape in the discrete element method[J], Granular Matter 9 (1-2) (2006) 69–80.
[44] H. Li, G.R. McDowell, Discrete element modelling of under sleeper pads using a box test[J], Granular Matter 20 (2) (2018) 26.
[45] X. Zhang, C. Zhao, W. Zhai, et al., Discrete element simulation and its validation on vibration and deformation of railway ballast[J], Rock and Soil Mechanics 38 (005) (2017) 1481–1488. In Chinese.
[46] H. Boler, Y.u. Qian, E. Tutumluer, Influence of size and shape properties of railroad ballast on aggregate packing: statistical analysis[J], Transp. Res. Rec. 2448 (1) (2014) 94–104.
[47] M. Koohmishi, M. Palassi, Effect of particle size distribution and subgrade condition on degradation of railway ballast under impact loads[J], Granular Matter 19 (3) (2017) 63.
[48] J. Kim, B.-S. Park, S.I. Woo, Y.-T. Choi, Evaluation of ballasted-track condition based on aggregate-shape characterization[J], Constr. Build. Mater. 232 (2020) 117082, https://doi.org/10.1016/j.conbuildmat.2019.117082.
[49] Ministry of Railways of the people's Republic of China. TB / T 2140-2008 railway ballast [S]. Beijing, 2008. (In Chinese).
[50] National Railway Administration of P.R. China. Code for design of high speed railways 2014 China Railway Press Beijing. (In Chinese).
[51] B.o. Wang, U. Martin, S. Rapp, Discrete element modeling of the single-particle crushing test for ballast stones[J], Comput. Geotech. 88 (2017) 61–73.
[52] S. Laryea, M. Safari Baghsorkhi, J.-F. Ferellec, G.R. McDowell, C. Chen, Comparison of performance of concrete and steel sleepers using experimental and discrete element methods[J], Transp. Geotech. 1 (4) (2014) 225–240.
[53] H. Jiang, X. Bian, C. Cheng, et al., Simulating train moving loads in physical model testing of railway infrastructure and its numerical calibration [J], Acta Geotech. 11 (2016) 231–242.
[54] X. Bian, H. Jiang, Y. Chen, J. Jiang, J. Han, A full-scale physical model test apparatus for investigating the dynamic performance of the slab track system of a high-speed railway [J], Proceedings of the Institution of Mechanical Engineers, Part F: Journal of Rail and Rapid Transit 230 (2) (2016) 554–571.
[55] X. Bian, W. Li, Y.u. Qian, E. Tutumluer, Analysing the effect of principal stress rotation on railway track settlement by discrete element method [J], Geotechnique 70 (9) (2020) 803–821.
[56] H. Jiang, X. Bian, X. Xu, et al., Full-scale model tests on dynamic performances of ballastless high-speed railways under moving train loads[J], Chinese Journal of Geotechnical Engineering 36 (002) (2014) 354–362. In Chinese.
[57] J.R. Edwards, Z. Gao, H.E. Wolf, M.S. Dersch, Y.u. Qian, Quantification of concrete railway sleeper bending moments using surface strain gauges[J], Measurement 111 (2017) 197–207.
[58] Jiang H. Dynamic interaction of slab track structure-subgrade system and accumulative settlement in high-speed railways [D]. Zhejiang University, 2014. (In Chinese).
[59] J. Lackenby, B. Indraratna, G. McDowell, D. Christie, Effect of confining pressure on ballast degradation and deformation under cyclic triaxial loading[J], Géotechnique 57 (6) (2007) 527–536.
[60] Q.D. Sun, B. Indraratna, S. Nimbalkar, Deformation and Degradation Mechanisms of Railway Ballast under High Frequency Cyclic Loading[J], J. Geotech. Geoenviron. Eng. 142 (1) (2016) 04015056, https://doi.org/10.1061/(ASCE)GT.1943-5606.0001375.
[61] Woodward P, Medero G, Griffiths D. Reducing track faults using polymer geocomposite technology[C]//Bearing Capacity of Roads, Railways and Airfields. 8th International Conference (BCR2A'09). 2009, 2: 1273-1282.
[62] P.K. Woodward, J. Kennedy, G.M. Medero, M. Banimahd, Application of in situ polyurethane geocomposite beams to improve the passive shoulder resistance of railway track[J], Proceedings of the Institution of Mechanical Engineers, Part F: Journal of Rail and Rapid Transit 226 (3) (2012) 294–304.
[63] P.K. Woodward, O. Laghrouche, A. El-kacimi, Railway track transition dynamics and reinforcement using polyurethane geocomposites[J], Geotechnical Engineering 45 (1) (2014) 28–38.
[64] Z. Shen, M. Jiang, DEM simulation of bonded granular material. Part II: extension to grain-coating type methane hydrate bearing sand[J], Comput. Geotech. 75 (2016) 225–243.
[65] H. Xiao, Z. Zhang, X. Cui, F. Jin, Experimental study and discrete element analysis of ballast bed with various sand content[J], Constr. Build. Mater. 271 (2021) 121869, https://doi.org/10.1016/j.conbuildmat.2020.121869.
[66] S. Tian, B. Indraratna, L. Tang, Y. Qi, X. Ling, A semi-empirical elasto-plastic constitutive model for coarse-grained materials that incorporates the effects of freeze-thaw cycles[J], Transp. Geotech. 24 (2020) 100373, https://doi.org/10.1016/j.trgeo.2020.100373.